

# Multiscale Modeling of Fatigue for Ductile Materials

Caglar Oskay and Jacob Fish

*Civil and Environmental Engineering Department  
Rensselaer Polytechnic Institute, Troy, NY, 12180, USA*

## Abstract

A multiscale model is developed for fatigue life predictions of elastoplastic solids and structures. The fatigue problem is formulated using a variant of the mathematical homogenization theory developed to account for almost periodic fields. Multiple temporal scales are employed to resolve the solution within a load cycle as well as to predict the useful life span of a structural component. The concept of almost-periodicity is introduced to account for irreversible inelastic deformation, which gives rise to nonperiodic fields in time domain. By this approach the original initial boundary value problem is decomposed into coupled micro-chronological (fast time-scale) and macro-chronological (slow time-scale) problems. The proposed life prediction methodology was implemented in ABAQUS and verified against the direct cycle-by-cycle simulation.

*Keywords:* temporal homogenization, almost periodicity, fatigue life prediction, multiscale modeling, ductile crack growth.

## 1 Introduction

The phenomenon of fatigue inherently involves multiple temporal and spatial scales. Multiple temporal scales exist due to the disparity between the period of a single load cycle acting on a structural component, which may be in the order of seconds, and the overall design life, which may span years. Likewise, multiple spatial scales exist due to the presence of micro-size cracks or inclusions with respect to the large size of the component of interest. Given this tremendous disparity of spatial and temporal scales, life predictions pose a great challenge to mechanics and materials communities.

While fatigue life prediction methods range from experimentation to modeling, the primary design tool today is experimental, based on so-called S-N (in case of high cycle fatigue) and  $\epsilon$ -N (in case of low cycle fatigue) curves, which relate the component life to cyclic stress or strain. Fatigue experiments are generally limited to specimens or small structural components, and therefore, boundary and initial conditions between the interconnect and the remaining structure requires some sort of modeling.

Paris's law [1] represents one of the first attempts to empirically model fatigue life. It states that under ideal conditions of high cycle fatigue (or small scale yielding) and constant amplitude

loading, the growth rate of long cracks depends on the amplitude of the stress intensity factors (for various variants, see [2, 3, 4, 5, 6]). Obviously, these ideal conditions do not exist in practice. Even under ideal cyclic loading conditions, the crack tip does not experience cyclic stress amplitude due to changing fracture mode caused by crack propagation and interaction between cracks.

Temporal scales can be resolved by means of cycle-by-cycle simulation, which has been recently reported (e.g., [7, 8]) in conjunction with cohesive zone models. Cycle-by-cycle simulation, however, may not be feasible for large systems undergoing large number of cycles. A so-called "cycle jump" technique [9, 10, 11] can be used to bridge the time scales. Although this approach has been shown to be effective to simulate the evolution of state variables, the governing equations are not guaranteed to be satisfied.

In this manuscript, a multiscale fatigue life prediction methodology is developed for both, the ductile and brittle materials. The proposed methodology is based on the generalization of the mathematical homogenization theory to account for non-periodicity in time domain. The non-periodicity is a byproduct of irreversible processes, such as damage accumulation, which naturally violates the condition of temporal periodicity. In this manuscript, the non-periodic contribution is modeled as an order  $\zeta \ll 1$  perturbation to the periodic field. Since the periodic fields are assumed to be of order one and the nonperiodic contribution of order  $\zeta \ll 1$  the resulting formulation is coined as the temporal homogenization for almost periodic fields. The theory presented here differs from the classical mathematical homogenization in two respects:

1. In contrast to the classical (spatial or temporal) homogenization theory, the local fields are allowed to deviate from the condition of local periodicity. The almost periodicity means that at the neighboring points homologous by periodicity, the value of a response function may have a variation of order  $\zeta \ll 1$ .
2. A two-term order one (macro- and micro-chronological) expansion is used to approximate the displacement field. This is in contrast to the classical homogenization where the micro-chronological contribution is of order  $\zeta$  (and thus giving rise to order one contribution in the derivatives). In a typical fatigue problem both the oscillatory field and the nonperiodic field resulting for example from the dead or live load could be of the same order and thus the corresponding displacements should be of the same order as well.

The present manuscript builds on the previous work of the authors [12] on high-cycle fatigue life predictions for brittle materials where the response fields were modeled as locally periodic ( $\tau$ -periodicity) whereas the state variables (i.e., state of damage) were assumed to be almost- $\tau$ -periodic. In the low-cycle fatigue considered in the present manuscript, all fields are modeled as almost periodic.

Nonperiodic fields were considered in a number of other engineering applications, particularly for the analysis of composite media with randomly distributed inclusions using stochastic [13, 14, 15, 16] and deterministic approaches [17, 18, 19, 20, 21], as well as for graded and stratified composites [22]. From the mathematical perspective, non-periodicity and almost periodicity with the associated convergence relations have been investigated and reported in a number of articles and monographs mainly in the field of spatial homogenization [23, 24, 25, 26, 27].

The multiscale fatigue model is developed for the case of accumulation of damage (microvoids) in the presence of elastoplastic effects, and propagation of macrocracks up to failure. Distributed damage is modeled using a modified Gurson's (GTN) model [28]. Damage accumulation is characterized by the nucleation, growth and coalescence of microvoids [28]. Kinematic hardening and

irreversible damage are incorporated into the model to generate a hysteretic behavior and to prevent shakedown and premature crack arrest. The propagation of cracks is simulated by the void growth and coalescence which is a precursor to strain softening, and loss of ellipticity resulting in mesh sensitivity. A number of localization limiters are known (e.g., [29, 30, 31, 32, 33]), but this issue is not addressed in the present paper.

The remaining of this manuscript is organized as follows. Section 2 addresses the fundamental aspects of the temporal homogenization in the presence of almost periodic fields. The problem statement for the fatigue life prediction analysis of ductile solids based on the GTN model is given in Section 3. Section 4 presents the formulation of the proposed multiscale methodology. Section 5 focuses on computational issues. Verification studies are given in Section 6. In Section 7, future research directions are discussed.

## 2 Multiple temporal scales with almost periodic functions

Multiple temporal scales are introduced to model slow degradation of material properties due to fatigue loading and the resulting crack propagation, as well as to resolve the deformation within a single load cycle. A *macro-chronological* scale, denoted by the intrinsic time coordinate,  $t$ , and a *micro-chronological* scale, denoted by the fast time coordinate,  $\tau$ , are introduced. These two scales are related through a small positive scaling parameter,  $\zeta$ :

$$\tau = \frac{t}{\zeta}; \quad 0 < \zeta \ll 1 \quad (1)$$

where, the scaling parameter,  $\zeta$ , is defined by the ratio:

$$\zeta = \frac{\tau_0}{t_r} \quad (2)$$

in which,  $t_r$  and  $\tau_0$  are the characteristic lengths of the macro- and the micro-chronological scales, respectively. The response fields, denoted by  $\phi$ , are assumed to depend on the multiple temporal scales:

$$\phi^\zeta(\mathbf{x}, t) = \phi(\mathbf{x}, t, \tau(t)) \quad (3)$$

where, superposed  $\zeta$  denotes a rapidly oscillating function in time; and  $\mathbf{x}$  is the spatial coordinates. Time differentiation in the presence of multiple temporal scales directly follows from the chain rule:

$$\dot{\phi}^\zeta(\mathbf{x}, t) = \dot{\phi}(\mathbf{x}, t, \tau) = \phi_{,t}(\mathbf{x}, t, \tau) + \frac{1}{\zeta} \phi_{,\tau}(\mathbf{x}, t, \tau) \quad (4)$$

in which, the comma followed by a subscript coordinate denotes partial derivative; and superposed dot is a total time derivative.

In the classical (spatial) homogenization theory [34], the response fields are commonly considered to be locally periodic. Local periodicity implies that at the neighboring points in the macro-domain, homologous by periodicity, the value of a response function is the same, but at different points in the macro-domain, the value of the function can be different. In the temporal homogenization analysis of structures under fatigue loads, the state of the structure or component is characterized by the accumulation of damage, which is generally irreversible in nature due to thermodynamic effects. Therefore, the associated response fields cannot be modeled using the

classical framework of local periodicity. Instead, we introduce the concept of *almost periodicity* to study fatigue response of ductile materials. The almost periodicity implies that, at the neighboring points in a spatial or temporal domain homologous by periodicity, the change in the value of a response function could be of order  $\zeta$ . Figure 1 depicts an example of the almost periodic function in time domain.

The basic properties of the almost periodic functions are subsequently discussed. We define a space,  $\mathcal{T}$ , consisting of all response functions, which can be represented in the form:

$$\phi_{ap}(\mathbf{x}, t, \tau) = \phi_p(\mathbf{x}, t, \tau) + \zeta \tau \bar{\phi}(\mathbf{x}) \quad (5)$$

The  $\kappa$ -periodic function,  $\phi_p(\mathbf{x}, t, \tau)$ , has the following property:

$$\phi_p(\mathbf{x}, t, \tau + k\kappa) - \phi_p(\mathbf{x}, t, \tau) = 0; \quad k \in \mathbb{N} \quad (6)$$

Setting  $\phi_p^\zeta(\mathbf{x}, t) = \phi_p(\mathbf{x}, t, t/\zeta)$ , the following relation exist [35]:

$$\lim_{\zeta \rightarrow 0} \int_{T^\zeta} \phi_p^\zeta(\mathbf{x}, t) dt \rightarrow \int_T \langle \phi_p(\mathbf{x}, t, \tau) \rangle dt \quad (7)$$

for any closed  $T \in \mathbb{R}$ . The periodic temporal homogenization (PTH) operator,  $\langle \cdot \rangle$ , is defined as:

$$\langle \cdot \rangle = \frac{1}{|\kappa|} \int_\kappa (\cdot) d\tau \quad (8)$$

It is important to note that the almost periodic function,  $\phi_{ap}$  does not satisfy (7):

$$\lim_{\zeta \rightarrow 0} \int_{T^\zeta} \phi_{ap}^\zeta dt = \lim_{\zeta \rightarrow 0} \int_{T^\zeta} \phi_p^\zeta dt + \bar{\phi} \frac{t^2}{2} \Big|_T \quad (9a)$$

$$\int_T \left( \frac{1}{|\kappa|} \int_\kappa \phi_{ap} d\tau \right) dt = \int_T \langle \phi_p \rangle dt + \frac{\zeta}{2} \frac{\bar{\phi}}{|\kappa|} \tau^2 \Big|_\kappa t \Big|_T \quad (9b)$$

or in other words, in the asymptotic limit  $\phi_{ap}$  does not weakly converge to  $\langle \phi_{ap} \rangle$ .

This serves as a motivation to defining the almost periodic temporal homogenization (APTH) operator, denoted as  $\mathfrak{M}(\phi)$ :

$$\mathfrak{M}(\phi)_{,t}(\mathbf{x}, t) = \langle \dot{\phi} \rangle(\mathbf{x}, t) \quad (10)$$

so that the weak convergence statement (7) can be extended to almost periodic functions in  $\mathcal{T}$ , i.e.,

$$\lim_{\zeta \rightarrow 0} \int_{T^\zeta} \phi_{ap}^\zeta dt \rightarrow \int_T \mathfrak{M}(\phi_{ap}(\mathbf{x}, t, \tau)) dt \quad (11)$$

where,  $\phi_{ap}^\zeta(\mathbf{x}, t) = \phi_{ap}(\mathbf{x}, t, t/\zeta)$ . Substituting (5) into the right hand side, and using (7), it can be easily seen that relation (11) is satisfied for all  $\phi_{ap} \in \mathcal{T}$ :

$$\begin{aligned} \int_T \mathfrak{M}(\phi_{ap}) dt &= \int_T \left( \int \left[ \frac{1}{\zeta} \langle \phi_{ap, \tau} \rangle + \langle \phi_{ap} \rangle_{,t} \right] dt \right) dt = \int_T \left( \int \left[ \bar{\phi} + \langle \phi_p \rangle_{,t} \right] dt \right) dt \\ &= \int_T (t \bar{\phi} + \langle \phi_p \rangle) = \int_T \phi_p dt + \bar{\phi} \frac{t^2}{2} \Big|_T \end{aligned} \quad (12)$$

Figure 2 depicts an example of the almost periodic fields. It compares the classical averaging operator,  $\langle \phi \rangle$  defined by Eq. 8 with an average function for almost periodic field,  $\mathfrak{M}(\phi)$ , defined by the APTH operator in 10. It can be clearly seen that  $\langle \phi \rangle$  fails to track the average response of the almost periodic function, whereas the APTH operator does precisely that. Further discussion follows in Section 4.

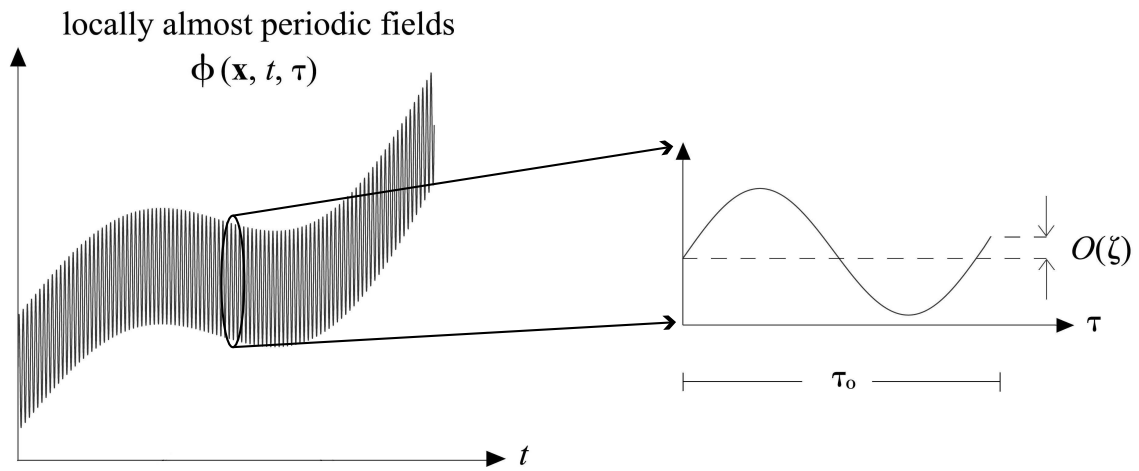


Figure 1: A locally almost periodic response field in time.

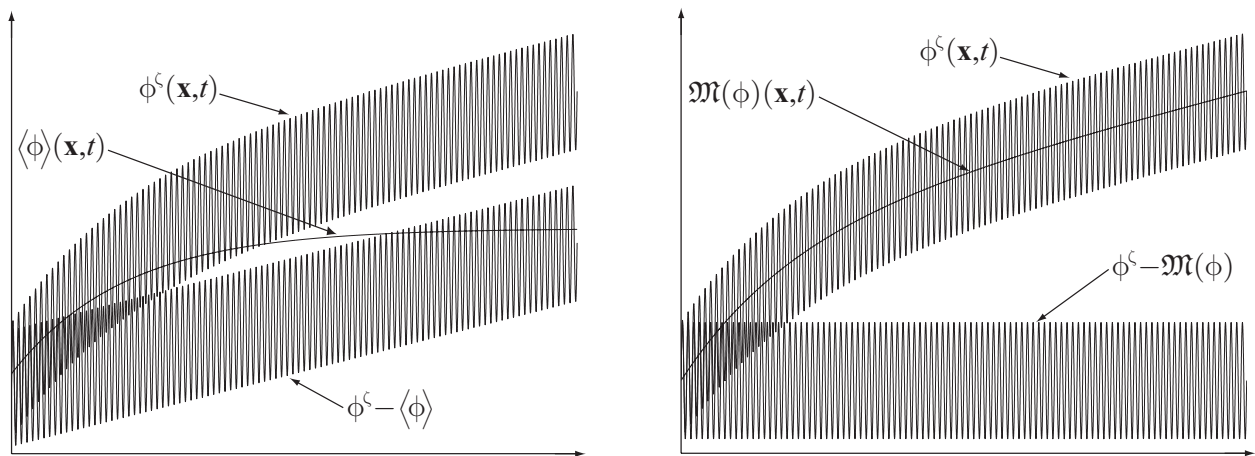


Figure 2: Decomposition of the response fields with respect to periodic and almost periodic temporal homogenization operators.

### 3 Problem statement

Progressive damage of elastoplastic materials caused by void nucleation and growth is commonly idealized using Gurson's model [36]. Gurson's model is a phenomenological model of combined damage and plasticity formulated based on limit analysis of a hollow spherical void embedded in the Von-Mises matrix material. A number of studies have been conducted over the years to assess the micro-mechanical and localization characteristics [37, 38] of the original model [36], and modifications have been proposed to improve its predictions by incorporating void nucleation [39] and coalescence [40], hardening characteristics [41, 42], void shape effects [43] and others. The state-of-the-art today is the so-called Gurson-Tvergaard-Needlemen (GTN) model, which has been validated for predicting the response of porous ductile materials under monotonic [44] as well as for cyclic [45, 46] loading conditions.

The initial boundary value problem for the damage process of ductile materials using the GTN model may be written as:

$$\text{Equilibrium equation: } \nabla \cdot \boldsymbol{\sigma}^\zeta + \mathbf{b}^\zeta = \mathbf{0} \quad \text{on } \Omega \times (0, t_0) \quad (13)$$

$$\text{Constitutive equation: } \dot{\boldsymbol{\sigma}}^\zeta = \mathbf{L} : (\dot{\boldsymbol{\epsilon}}^\zeta - \dot{\boldsymbol{\mu}}^\zeta) \quad \text{on } \Omega \times (0, t_0) \quad (14)$$

$$\text{Kinematic equation: } \boldsymbol{\epsilon}^\zeta = \frac{1}{2} (\nabla \mathbf{u}^\zeta + \mathbf{u}^\zeta \nabla) \quad \text{on } \Omega \times (0, t_0) \quad (15)$$

$$\text{Initial condition: } \mathbf{u}^\zeta = \mathbf{u}' \quad \text{on } \Omega \quad (16)$$

$$\text{Boundary conditions: } \mathbf{u}^\zeta = \bar{\mathbf{u}}^\zeta \quad \text{on } \Gamma_u \times (0, t_0) \quad (17)$$

$$\mathbf{n} \boldsymbol{\sigma}^\zeta = \mathbf{t}^\zeta \quad \text{on } \Gamma_t \times (0, t_0) \quad (18)$$

with the usual assumption of additive split:

$$\boldsymbol{\epsilon}^\zeta = \mathbf{e}^\zeta + \boldsymbol{\mu}^\zeta \quad (19)$$

where,  $\mathbf{u}^\zeta$  is the displacement vector;  $\boldsymbol{\sigma}^\zeta$  is the Cauchy stress tensor;  $\boldsymbol{\epsilon}^\zeta$ ,  $\mathbf{e}^\zeta$ , and,  $\boldsymbol{\mu}^\zeta$ , are the total, elastic and plastic strain tensors, respectively;  $\mathbf{L}$  is the tensor of elastic moduli;  $\nabla$  is the vector differential operator given by  $\nabla = (\partial/\partial x_1, \partial/\partial x_2, \partial/\partial x_3)$  in Cartesian coordinate system;  $\mathbf{b}^\zeta$  is the body force;  $\Omega$  and  $\Gamma$  are the spatial problem domain and its boundary, respectively;  $\mathbf{u}'$  is the initial displacement field;  $\bar{\mathbf{u}}^\zeta$  and  $\mathbf{t}^\zeta$  are the prescribed displacements and tractions on the boundaries  $\Gamma_u$  and  $\Gamma_t$ , respectively, where  $\Gamma = \Gamma_u \cup \Gamma_t$  and  $\Gamma_u \cap \Gamma_t = \emptyset$ . For simplicity, analysis is restricted to small deformations.

The yield function of the GTN model with mixed hardening is expressed as:

$$\Phi^\zeta \equiv \Phi^\zeta(\boldsymbol{\sigma}^\zeta, \mathbf{H}^\zeta) = \frac{(\bar{q}^\zeta)^2}{(\sigma_F^\zeta)^2} + 2q_1 \hat{f}^\zeta \cosh\left(-\frac{3}{2}q_2 \frac{\bar{p}^\zeta}{\sigma_F^\zeta}\right) - 1 - (q_1 \hat{f}^\zeta)^2 = 0 \quad (20)$$

where,  $\mathbf{H}$  denotes the set of internal state variables;  $q_1$  and  $q_2$  are the Tvergaard constants;

$$\bar{q}^\zeta = \sqrt{\frac{3}{2} \bar{\mathbf{s}}^\zeta : \bar{\mathbf{s}}^\zeta}, \quad \bar{\mathbf{s}}^\zeta = \boldsymbol{\Theta}^\zeta + \bar{p}^\zeta \boldsymbol{\delta}, \quad \boldsymbol{\Theta}^\zeta = \boldsymbol{\sigma}^\zeta - \boldsymbol{\alpha}^\zeta, \quad \bar{p}^\zeta = -\frac{1}{3} \boldsymbol{\Theta}^\zeta : \boldsymbol{\delta} \quad (21)$$

where,  $\boldsymbol{\alpha}^\zeta$  is the center of the yield surface; and  $\boldsymbol{\delta}$  is the second order identity tensor. The radius of the yield surface of the matrix material,  $\sigma_F^\zeta$ , is defined as [41]:

$$\sigma_F^\zeta = (1 - b)\sigma_y + b\sigma_M \quad (22)$$

where,  $\sigma_y$  and  $\sigma_M^\zeta$  are the initial yield and matrix flow stresses, respectively; and  $b \in [0, 1]$  is a constant.  $b = 1$ ,  $b = 0$ , and  $b \in ]0, 1[$  correspond to the pure isotropic, kinematic, and mixed hardening conditions, respectively.

The void coalescence function,  $\hat{f}^\zeta(f^\zeta)$ , is introduced to predict the loss of material stress carrying capacity at a realistic state of void volume fraction. Following Tvergaard [40], the void coalescence is modeled using the piecewise linear function:

$$\hat{f}^\zeta = \begin{cases} f^\zeta & f^\zeta < f_c \\ f_c + \left(\frac{1}{q_1} - f_c\right) \frac{f^\zeta - f_c}{f_f - f_c} & f^\zeta \geq f_c \end{cases} \quad (23)$$

in which, critical void volume fraction,  $f_c$ , and void volume fraction at failure,  $f_f$ , are material parameters. When  $f^\zeta$  approaches  $f_f$ ,  $\hat{f}^\zeta \rightarrow 1/q_1$ , and the material loses its stress carrying capacity.

At a material point, the void volume fraction is allowed to grow due to the nucleation of new, as well as the growth of existing voids. The evolution equation of the void volume fraction may be then written as:

$$\dot{f}^\zeta = \dot{f}_{\text{growth}}^\zeta + \dot{f}_{\text{nucleation}}^\zeta \quad (24)$$

The rate of growth of the void volume fraction is non-zero only after the onset of plastic yielding under tensile loading:

$$\dot{f}_{\text{growth}}^\zeta = (1 - f^\zeta) \langle \dot{\boldsymbol{\mu}}^\zeta : \boldsymbol{\delta} \rangle_+ \quad (25)$$

where,  $\langle \cdot \rangle_+ = [(\cdot) + |\cdot|]/2$  are MacCauley brackets. MacCauley brackets are introduced to avoid closure of voids under compressive stress, which may otherwise prevent damage accumulation in some loading conditions, such as when the material experiences yielding in both tension and compression within a single load cycle. In this study, a plastic strain controlled void nucleation is adopted [39]:

$$\dot{f}_{\text{nucleation}}^\zeta = \mathcal{A}^\zeta(\rho^\zeta) \dot{\rho}^\zeta \quad (26)$$

where,  $\mathcal{A}^\zeta$  is taken to have a normal distribution:

$$\mathcal{A}^\zeta(\rho^\zeta) = \frac{f_N}{s_N \sqrt{2\pi}} \exp \left\{ -\frac{1}{2} \left( \frac{\rho^\zeta - \varepsilon_N}{s_N} \right)^2 \right\} \quad \text{if } \rho^\zeta > 0, \quad \dot{\boldsymbol{\mu}}^\zeta : \boldsymbol{\delta} > 0 \quad (27)$$

in which,  $\rho^\zeta$  is the equivalent plastic strain; material parameter,  $f_N$ , is the volume fraction of void nucleating particles;  $\varepsilon_N$  is the mean strain for nucleation; and  $s_N$  is the standard deviation of nucleation.

The rate of the effective plastic strain is formulated based on the postulate that the rate of plastic work of the matrix material is equivalent to the plastic work rate of the entire unit cell:

$$\dot{\rho}^\zeta = \frac{\boldsymbol{\Theta}^\zeta : \boldsymbol{\mu}^\zeta}{(1 - f^\zeta) \sigma_F^\zeta} \quad (28)$$

The equivalent plastic strain rate is related to the matrix flow strength using the following equation:

$$\dot{\sigma}_M^\zeta = \left( \frac{E E_t}{E - E_t} \right) \dot{\rho}^\zeta = E^t \dot{\rho}^\zeta \quad (29)$$

in which  $E$  is the Young's modulus; and  $E_t$  is the tangent to the uniaxial true stress- natural strain diagram at a given stress level. The uniaxial stress-strain diagram at a given stress level.

The plastic part of the strain rate is chosen to follow the normality rule:

$$\dot{\boldsymbol{\mu}}^\zeta = \lambda^\zeta \frac{\partial \Phi^\zeta}{\partial \boldsymbol{\sigma}^\zeta}; \quad \lambda^\zeta \geq 0 \quad (30)$$

in which,  $\lambda^\zeta$  is the consistency parameter. The evolution equation for the yield surface motion is expressed using Ziegler's hardening rule:

$$\dot{\boldsymbol{\alpha}}^\zeta = \vartheta^\zeta \boldsymbol{\Theta}^\zeta; \quad \vartheta^\zeta \geq 0 \quad (31)$$

The consistency parameters,  $\lambda^\zeta$  and  $\vartheta^\zeta$  are evaluated by employing the usual complementary and consistency conditions.

## 4 Multiple temporal scale analysis

We start by expanding the response fields using the dual decomposition:

$$\phi(\mathbf{x}, t, \tau) = \phi^o(\mathbf{x}, t) + \phi^1(\mathbf{x}, t, \tau) \quad (32a)$$

$$= \mathfrak{M}(\phi)(\mathbf{x}, t) + \tilde{\phi}(\mathbf{x}, t, \tau) \quad (32b)$$

in which,  $\phi$  denotes the response fields (displacement, strain, stress) or internal state variables. Equation (32) is defined such that:

$$\langle \phi^1(\mathbf{x}, t, \tau) \rangle = 0 \quad (33)$$

Employing the definition of the APTH operator given by (10), and dual decompositions (32), the following relations can be inferred:

$$\tilde{\phi}_{,\tau} = \phi_{,\tau}^1, \quad \langle \tilde{\phi} \rangle_{,t} = -\frac{1}{\zeta} \langle \tilde{\phi}_{,\tau} \rangle, \quad \tilde{\phi} = \phi^1 - \mathfrak{M}(\phi^1), \quad \mathfrak{M}(\phi^o) = \phi^o \quad (34)$$

In view of the above definitions, the original boundary value problem is sought to be decomposed into coupled macro-chronological (homogenized) and micro-chronological (cell) boundary value problems. In what follows, the decompositions of the kinematic conditions, equilibrium equations, constitutive relations, and initial and boundary conditions are presented.

The strain tensor may be decomposed by applying (32) to the displacement field, substituting the resulting fields into (15), and exploiting the linearity of the PTH and APTH operators:

$$\boldsymbol{\epsilon}^m = \frac{1}{2} (\nabla \mathbf{u}^m + \mathbf{u}^m \nabla); \quad m = 0, 1 \quad (35)$$

$$\mathfrak{M}(\boldsymbol{\epsilon}) = \frac{1}{2} (\nabla \mathfrak{M}(\mathbf{u}) + \mathfrak{M}(\mathbf{u}) \nabla), \quad \tilde{\boldsymbol{\epsilon}} = \frac{1}{2} (\nabla \tilde{\mathbf{u}} + \tilde{\mathbf{u}} \nabla) \quad (36)$$

Applying (32a) to the stress, strain, and the plastic strain fields, substituting the resulting equations into the elastoplastic constitutive equation, exploiting the dual decomposition relation (34a), and gathering the terms of the same order yields:

$$O(\zeta^{-1}): \quad \tilde{\boldsymbol{\sigma}}_{,\tau} = \mathbf{L} : (\tilde{\boldsymbol{\epsilon}}_{,\tau} - \tilde{\boldsymbol{\mu}}_{,\tau}) \quad \text{on } \Omega \times (0, \tau_o) \quad (37a)$$

$$O(1): \quad \boldsymbol{\sigma}_{,t}^o + \boldsymbol{\sigma}_{,t}^1 = \mathbf{L} : (\boldsymbol{\epsilon}_{,t}^o + \boldsymbol{\epsilon}_{,t}^1 - \boldsymbol{\mu}_{,t}^o - \boldsymbol{\mu}_{,t}^1) \quad (37b)$$

The constitutive equation for the micro-chronological problem is given by (37a). The macro-chronological constitutive relation is obtained by applying the PTH operator to (37), employing (33), and exploiting the definition of the APTH operator:

$$\mathfrak{M}(\boldsymbol{\sigma})_{,t} = \mathbf{L} : \left( \mathfrak{M}(\boldsymbol{\epsilon})_{,t} - \mathfrak{M}(\boldsymbol{\mu})_{,t} \right) = \mathbf{L} : \left[ \frac{1}{\zeta} \left( \langle \tilde{\boldsymbol{\epsilon}}_{,\tau} \rangle - \langle \tilde{\boldsymbol{\mu}}_{,\tau} \rangle \right) + \boldsymbol{\epsilon}_{,t}^o - \boldsymbol{\mu}_{,t}^o \right] \quad \text{on } \Omega \times (0, t_o) \quad (38)$$

Next, we formulate the evolution equations for the micro- and macro-chronological problems. The consistency parameter of the flow rule,  $\lambda$ , is evaluated using the consistency condition which involves rate relations (i.e.,  $\dot{\Phi} = 0$ ). At a specified material point,  $\mathbf{x}$ , the following two-scale expansion is employed:

$$\lambda(t, \tau) = \frac{1}{\zeta} \lambda^1(t, \tau) + \lambda^o(t) \quad (39)$$

in which,  $\lambda^1$  and  $\lambda^o$  may be interpreted as consistency parameters induced by the micro- and macro-chronological loadings, respectively. The yield condition may be expressed in terms of the micro- and macro-chronological fields:

$$\Phi(t, \tau) \equiv \Phi(\boldsymbol{\sigma}, \mathbf{H}) = \Phi(\mathfrak{M}(\boldsymbol{\sigma}), \tilde{\boldsymbol{\sigma}}, \mathfrak{M}(\mathbf{H}), \tilde{\mathbf{H}}) \quad (40)$$

Applying (32a) to the plastic strain tensor, substituting the resulting equation, as well as (39) and (40) into the flow rule (30), exploiting the dual decomposition relations, and separating the terms with respect to their orders yield:

$$O(\zeta^{-1}) : \quad \tilde{\boldsymbol{\mu}}_{,\tau} = \lambda^1 \frac{\partial \Phi}{\partial \boldsymbol{\sigma}} \quad (41a)$$

$$O(1) : \quad \boldsymbol{\mu}_{,t}^o + \boldsymbol{\mu}_{,t}^1 = \lambda^o \frac{\partial \Phi}{\partial \boldsymbol{\sigma}} \quad (41b)$$

The flow rule for the micro-chronological problem is given by (41a). The macro-chronological flow rule is obtained by applying the PTH operator to (41), and using the definition of the APTH operator:

$$\mathfrak{M}(\boldsymbol{\mu})_{,t} = \frac{1}{\zeta} \left\langle \lambda^1 \frac{\partial \Phi}{\partial \boldsymbol{\sigma}} \right\rangle + \lambda^o \left\langle \frac{\partial \Phi}{\partial \boldsymbol{\sigma}} \right\rangle \quad (42)$$

The consistency parameters for the micro- and macro-chronological problems are evaluated by employing the consistency condition of the original problem. Using the chain rule:

$$O(\zeta^{-1}) : \quad \Phi_{,\tau} = 0 \quad (43)$$

$$O(1) : \quad \Phi_{,t} = 0 \quad (44)$$

The micro-chronological consistency parameter is evaluated using (43):

$$\lambda^1 = \frac{1}{H} \frac{\partial \Phi}{\partial \boldsymbol{\sigma}} : \tilde{\boldsymbol{\sigma}}_{,\tau} \quad (45)$$

The evaluation of the hardening parameter,  $H$ , for the GTN model is presented in Appendix A.

The macro-chronological consistency parameter,  $\lambda^o$ , is evaluated by applying the PTH operator to (44), and using the definition of the APTH operator:

$$\lambda^o = \left\langle \frac{1}{H} \frac{\partial \Phi}{\partial \boldsymbol{\sigma}} \right\rangle : \mathfrak{M}(\boldsymbol{\sigma})_{,t} + \left\langle \frac{1}{H} \frac{\partial \Phi}{\partial \boldsymbol{\sigma}} : \tilde{\boldsymbol{\sigma}}_{,t} \right\rangle \quad (46)$$

The evolution equations of the internal state variables (22), (25), (26), (28), and (29) can be stated as:

$$\dot{\mathbf{H}} = \bar{\mathbf{h}}(\boldsymbol{\sigma}, \boldsymbol{\mu}, \mathbf{H}) \quad (47)$$

or in terms of the macro- and micro-chronological fields:

$$\dot{\mathbf{H}} = \mathbf{h}(\mathfrak{M}(\boldsymbol{\sigma}), \tilde{\boldsymbol{\sigma}}, \mathfrak{M}(\boldsymbol{\mu}), \tilde{\boldsymbol{\mu}}, \mathfrak{M}(\mathbf{H}), \tilde{\mathbf{H}}) \quad (48)$$

The evolution equations of the internal state variables can be expanded as:

$$\mathbf{h} = \frac{1}{\zeta} \mathbf{h}^1 + \mathbf{h}^0 \quad (49)$$

Applying (32a) to the right hand side of (48), using (49), and exploiting the dual decomposition relations (34) gives:

$$\tilde{\mathbf{H}}_{,\tau} = \mathbf{h}^1(\mathfrak{M}(\boldsymbol{\sigma}), \tilde{\boldsymbol{\sigma}}, \mathfrak{M}(\boldsymbol{\mu}), \tilde{\boldsymbol{\mu}}, \mathfrak{M}(\mathbf{H}), \tilde{\mathbf{H}}) \quad (50a)$$

$$\mathbf{H}_{,t}^0 = \mathbf{h}^0(\mathfrak{M}(\boldsymbol{\sigma}), \tilde{\boldsymbol{\sigma}}, \mathfrak{M}(\boldsymbol{\mu}), \tilde{\boldsymbol{\mu}}, \mathfrak{M}(\mathbf{H}), \tilde{\mathbf{H}}) \quad (50b)$$

The micro-chronological evolution equation for the internal state variables is given by (50a). The evolution equations for the macro-chronological problem is obtained by applying the PTH operator to (50) and exploiting the definition of the APTH operator:

$$\mathfrak{M}(\mathbf{H})_{,t} = \frac{1}{\zeta} \langle \mathbf{h}^1 \rangle + \langle \mathbf{h}^0 \rangle \quad (51)$$

The micro- and macro-chronological evolution equations of the internal state variables for the GTN model (i.e., evolution equations for void volume fraction, equivalent plastic strain, matrix flow stress, yield surface center and radius) are presented in Appendix A.

The equilibrium equation for the macro-chronological problem is evaluated by applying the APTH operator,  $\mathfrak{M}(\cdot)$ , to (13):

$$\nabla \cdot \mathfrak{M}(\boldsymbol{\sigma}) + \mathfrak{M}(\mathbf{b}) = \mathbf{0} \quad \text{on } \Omega \times (0, t_0) \quad (52)$$

The equilibrium equation for the micro-chronological problem is evaluated by applying (32b) to the stress tensor, inserting the expanded terms into (13), and subtracting (52) from the resulting equation, which gives:

$$\nabla \cdot \tilde{\boldsymbol{\sigma}} + \mathbf{b} - \mathfrak{M}(\mathbf{b}) = \mathbf{0} \quad \text{on } \Omega \times (0, \tau_0) \quad (53)$$

Finally, we seek to decompose the initial and boundary conditions of the source problem to obtain the initial and boundary conditions for the micro- and macro-chronological problems. Substituting the displacement and stress decompositions into (16)-(18), and applying the APTH operator yields the boundary and the initial conditions for the macro-chronological problem:

$$\text{Initial condition: } \mathfrak{M}(\mathbf{u})(\mathbf{x}, t=0) = \mathbf{u}'(\mathbf{x}) \quad \text{on } \Omega \quad (54)$$

$$\text{Boundary conditions: } \mathfrak{M}(\mathbf{u}) = \mathfrak{M}(\bar{\mathbf{u}}(\mathbf{x}, t, \tau)) \quad \text{on } \Gamma_u \times (0, t_0) \quad (55)$$

$$\mathbf{n} \mathfrak{M}(\boldsymbol{\sigma}) = \mathfrak{M}(\mathbf{t}(\mathbf{x}, t, \tau)) \quad \text{on } \Gamma_t \times (0, t_0) \quad (56)$$

Similarly, the micro-chronological initial and boundary conditions are obtained by applying (32b) to the displacement and stress fields, substituting the resulting equation into (16)-(18) and subtracting (54)-(56) from the resulting equations:

$$\text{Initial condition: } \tilde{\mathbf{u}}(\mathbf{x}, t, \tau = 0) = \mathbf{0} \quad \text{on } \Omega \quad (57)$$

$$\text{Boundary conditions: } \tilde{\mathbf{u}}(\mathbf{x}, t, \tau) = \bar{\mathbf{u}} - \mathfrak{M}(\bar{\mathbf{u}}) \quad \text{on } \Gamma_u \times (0, \tau_o) \quad (58)$$

$$\mathbf{n}\tilde{\boldsymbol{\sigma}}(\mathbf{x}, t, \tau) = \mathbf{t} - \mathfrak{M}(\mathbf{t}) \quad \text{on } \Gamma_t \times (0, \tau_o) \quad (59)$$

The macro-chronological (homogenized) and the micro-chronological (cell) problems are summarized in Box 1. It can be seen that the two problems are two-way coupled. The adaptive integration algorithm to evaluate the coupled micro- and macro-chronological problems is described in Section 5.

**Governing equations of the macro-chronological IBVP:**

$$\text{Equilibrium equation: } \nabla \cdot \mathfrak{M}(\boldsymbol{\sigma}) + \mathfrak{M}(\mathbf{b}) = \mathbf{0} \quad \text{on } \Omega \times (0, t_o)$$

$$\text{Constitutive equation: } \mathfrak{M}(\boldsymbol{\sigma})_{,t} = \mathbf{L} : \left( \mathfrak{M}(\boldsymbol{\epsilon})_{,t} - \mathfrak{M}(\boldsymbol{\mu})_{,t} \right) \quad \text{on } \Omega \times (0, t_o)$$

$$\text{Kinematic equation: } \mathfrak{M}(\boldsymbol{\epsilon}) = \frac{1}{2} (\nabla \mathfrak{M}(\mathbf{u}) + \mathfrak{M}(\mathbf{u}) \nabla) \quad \text{on } \Omega \times (0, t_o)$$

$$\text{Initial condition: } \mathfrak{M}(\mathbf{u})(\mathbf{x}, t = 0) = \mathbf{u}'(\mathbf{x}) \quad \text{on } \Omega$$

$$\text{Boundary conditions: } \mathfrak{M}(\mathbf{u}) = \mathfrak{M}(\bar{\mathbf{u}}(\mathbf{x}, t, \tau)) \quad \text{on } \Gamma_u \times (0, t_o)$$

$$\mathbf{n}\mathfrak{M}(\boldsymbol{\sigma}) = \mathfrak{M}(\mathbf{t}(\mathbf{x}, t, \tau)) \quad \text{on } \Gamma_t \times (0, t_o)$$

$$\text{Flow rule: } \mathfrak{M}(\boldsymbol{\mu})_{,t} = \frac{1}{\zeta} \left\langle \lambda^1 \frac{\partial \Phi}{\partial \boldsymbol{\sigma}} \right\rangle + \lambda^o \left\langle \frac{\partial \Phi}{\partial \boldsymbol{\sigma}} \right\rangle$$

$$\text{Evolution equations: } \mathfrak{M}(\mathbf{H})_{,t} = \frac{1}{\zeta} \langle \mathbf{h}^1 \rangle + \langle \mathbf{h}^o \rangle$$

**Governing equations of the micro-chronological IBVP:**

$$\text{Equilibrium equation: } \nabla \cdot \tilde{\boldsymbol{\sigma}} + \mathbf{b} - \mathfrak{M}(\mathbf{b}) = \mathbf{0} \quad \text{on } \Omega \times (0, \tau_o)$$

$$\text{Constitutive equation: } \tilde{\boldsymbol{\sigma}}_{,\tau} = \mathbf{L} : (\tilde{\boldsymbol{\epsilon}}_{,\tau} - \tilde{\boldsymbol{\mu}}_{,\tau}) \quad \text{on } \Omega \times (0, \tau_o)$$

$$\text{Kinematic equation: } \tilde{\boldsymbol{\epsilon}} = \frac{1}{2} (\nabla \tilde{\mathbf{u}} + \tilde{\mathbf{u}} \nabla) \quad \text{on } \Omega \times (0, \tau_o)$$

$$\text{Initial condition: } \tilde{\mathbf{u}}(\mathbf{x}, t, \tau = 0) = \mathbf{0} \quad \text{on } \Omega$$

$$\text{Boundary conditions: } \tilde{\mathbf{u}}(\mathbf{x}, t, \tau) = \bar{\mathbf{u}} - \mathfrak{M}(\bar{\mathbf{u}}) \quad \text{on } \Gamma_u \times (0, \tau_o)$$

$$\mathbf{n}\tilde{\boldsymbol{\sigma}}(\mathbf{x}, t, \tau) = \mathbf{t} - \mathfrak{M}(\mathbf{t}) \quad \text{on } \Gamma_t \times (0, \tau_o)$$

$$\text{Flow rule: } \tilde{\boldsymbol{\mu}}_{,\tau} = \lambda^1 \frac{\partial \Phi}{\partial \boldsymbol{\sigma}}$$

$$\text{Evolution equations: } \tilde{\mathbf{H}}_{,\tau} = \mathbf{h}^1(\mathfrak{M}(\boldsymbol{\sigma}), \tilde{\boldsymbol{\sigma}}, \mathfrak{M}(\boldsymbol{\mu}), \tilde{\boldsymbol{\mu}}, \mathfrak{M}(\mathbf{H}), \tilde{\mathbf{H}})$$

**Box 1:** Governing equations of the macro- and micro-chronological initial boundary value problems.

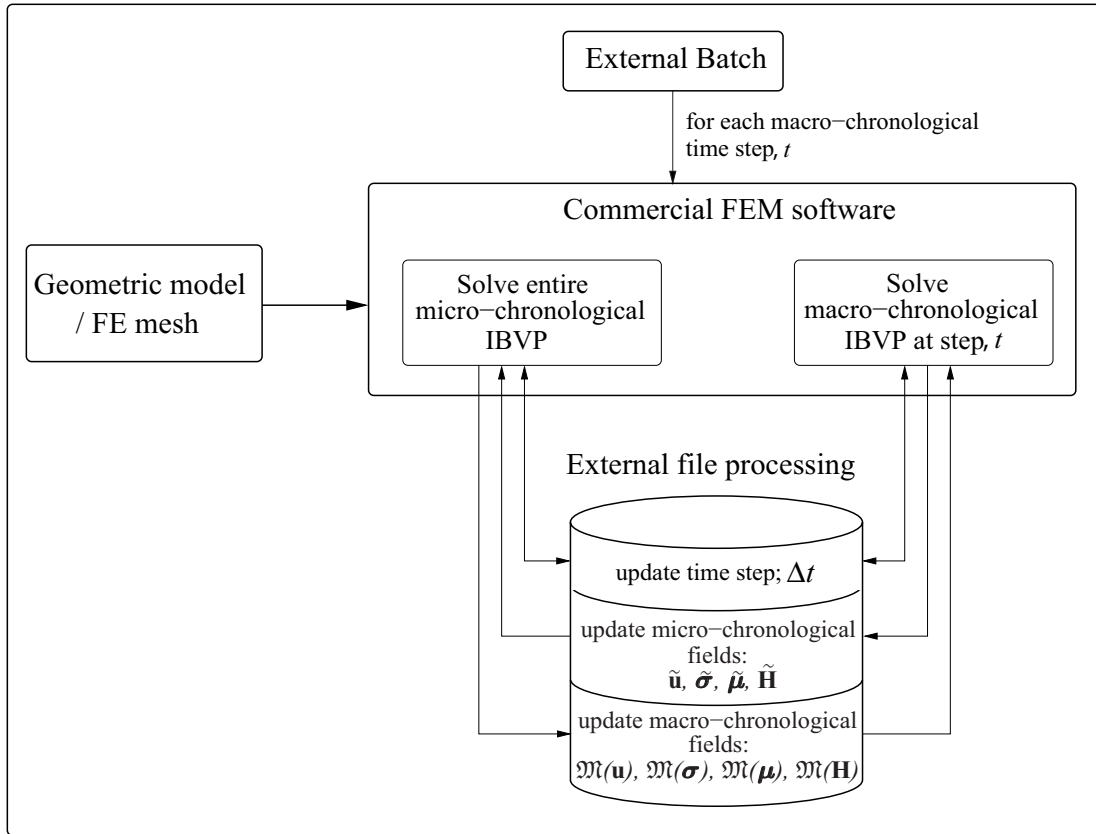


Figure 3: Schematic of the program architecture for the proposed multiscale fatigue life prediction method.

## 5 Implementation

In this section, the coupled micro- and macro-chronological IBVPs are evolved using the staggered adaptive integration algorithm described below.

Figure 3 displays the general structure of the proposed implementation of the multiscale analysis presented in Section 4. The execution of the analysis is controlled by external batch file, which, in turn invokes the execution of the conventional finite element program. The field and state variable information is transferred between the micro- and macro-chronological problems using external files stored on a hard disk. This specific structure of the implementation is selected to accommodate the use of commercial finite element packages. In this study, ABAQUS was employed to conduct the numerical simulations (Section 6). Appropriate user supplied subroutines (UMAT) were provided to integrate the constitutive models of the micro- and macro-chronological problems.

The stress updates of the two problems were conducted using the backward Euler algorithm for pressure dependent materials. The integration algorithm employed in this study is based on the method first proposed by Aravas [47], and further extended to include kinematic hardening by Lee and Zhang [48].

The accuracy and performance of the proposed multiscale evaluation of structural response under fatigue loading depends on the selection of the time step size for the macro-chronological

problem. The macro-chronological time step size is related to the number of skipped cycles by  $\Delta N = \Delta t / \tau_0$ . When the overall system response is rapidly changing in macro-chronological time, the step size must be selected to be relatively small to maintain accuracy. In contrast, when the overall system response is relatively smooth, the step size of the macro-chronological problem could be appropriately increased to reduce the total computational cost. This calls for adaptive selection of the macro-chronological time step. In the following we describe the adaptive incremental strategy for the coupled solution of the micro- and macro-chronological problems, (see Box 2).

The objective of the proposed adaptive algorithm is to incrementally evaluate the micro- and macro-chronological response fields  $\tilde{\phi}(\mathbf{x}, t, \tau)$  and  $\mathfrak{M}(\phi)(\mathbf{x}, t)$ , respectively, at a time  $t = t_{n+1}$ . The response fields at the previous time step,  $t = t_n$ , are assumed to be given, whereas at  $t_{n+1}$  they are assumed to be unknown. The macro-chronological step size,  $\Delta t$ , is evaluated by controlling the error in certain fields of interest, denoted by the vector,  $\boldsymbol{\omega}(\boldsymbol{\sigma}, \boldsymbol{\mu}, \mathbf{H})$ . In this study, the vector of the control variables is selected to include the void volume fraction,  $f$ , and the Euclidian norm of the plastic strain deviator,  $\mathbf{s}_\mu$ :

$$\boldsymbol{\omega} = \{f, \|\mathbf{s}_\mu\|_2\}^T; \quad \mathbf{s}_\mu = \boldsymbol{\mu} - \frac{1}{3}\boldsymbol{\delta} : \boldsymbol{\mu} \quad (60)$$

The integration error is defined as  $E_j^\omega = |_{(t_{n+1}; \Delta t)} \omega_j - _{(t_{n+1}; \Delta t/2)} \omega_j| \leq E_j^{tol}$  where,  $_{(t_{n+1}; \Delta t)} \boldsymbol{\omega}$  and  $_{(t_{n+1}; \Delta t/2)} \boldsymbol{\omega}$  are the control variables computed using the algorithm described in Box 2 with the integration step sizes  $\Delta t$  and  $\Delta t/2$ , respectively;  $E_j^{tol}$  are the error tolerances for the control variables (i.e., void volume fraction and the plastic strain deviator, respectively). The time step size,  $\Delta t$  is subsequently redefined to maintain accuracy (Box 2, steps 5-12).

For a given macro-chronological time step size,  $\Delta t$ , the macro-chronological response fields are updated using a two-step procedure. Figure 4 illustrates the basic structure of the proposed two-step scheme. First, the macro-chronological response fields are updated due to oscillatory (fatigue) loading from the previous converged state,  $_{t_n} \mathfrak{M}(\phi)$ , to obtain the intermediate configuration,  $\mathfrak{M}(\phi)^*$ , as shown in Box 2 (step 5). Next, the response fields are subjected to the macro-chronological load (dead or live load) and updated starting from the intermediate configuration,  $\mathfrak{M}(\phi)^*$ , to obtain the current state of response fields,  $\mathfrak{M}(\phi)$ , using one of the conventional stress integration algorithm (e.g., see [49]).

*Remark:* The piecewise linear void coalescence function,  $\hat{f}^\zeta(f^\zeta)$ , given by (23) has a discontinuity at its first derivative when the void volume fraction approaches the critical ratio,  $f_c$ . Numerical experiments indicate convergence difficulties around the discontinuity, especially when the time step size is large. A smooth void coalescence law, with a third order polynomial representation, was chosen to overcome this difficulty:

$$\hat{f}^\zeta = f^\zeta + \frac{6}{f_f^3} \left( \frac{1}{q_1} - f_f \right) \left[ \left( \frac{f_f}{2} - f_c \right) + \left( \frac{f_c}{f_f} - \frac{1}{3} \right) f^\zeta \right] (f^\zeta)^2 \quad (61)$$

Figure 5 shows the original Tvergaard [40] and the proposed void coalescence functions given in (23) and (61), respectively. The constants of the third order void coalescence law were chosen to minimize the error between the two models and to satisfy the boundary conditions. Similar to the original piecewise linear function, material loses its stress carrying capacity ( $\hat{f}^\zeta = 1/q_1$ ) as void volume fraction approaches  $f_f$ .

**Input:**  ${}_{t_n} \mathfrak{M}(\phi)(\mathbf{x})$  and  ${}_{t_n} \tilde{\phi}(\mathbf{x}, \tau)$

**Output:**  $\Delta t$ ,  ${}_{t_{n+1}} \mathfrak{M}(\phi)$  and  ${}_{t_{n+1}} \tilde{\phi}(\tau)$ .

(\* For simplicity, the subscript for the current values is often omitted (i.e.,  $\phi \equiv {}_{t_{n+1}} \phi$ ). \*)

1. Initialize:  $ID_{tol} \leftarrow \mathbf{false}$ ,  $E_F \leftarrow 1$
2. Compute  ${}_{t_n} \boldsymbol{\omega} \equiv \boldsymbol{\omega}({}_{t_n} \boldsymbol{\sigma}, {}_{t_n} \mathbf{H}, {}_{t_n} \boldsymbol{\mu})$  and  ${}_{t_n} \delta \boldsymbol{\omega}$  at each integration point:

$${}_{t_n} \delta \boldsymbol{\omega}(\mathbf{x}_k) = {}_{t_n} \boldsymbol{\omega}(\mathbf{x}_k, \tau_o) - {}_{t_n} \boldsymbol{\omega}(\mathbf{x}_k, 0); \quad \forall k \in 1, 2, \dots, n_{ip}$$

3. Compute initial estimate of  $\Delta t$ :

$$\Delta t = \inf_{j=1}^{n_{od}} \left( \text{int} \left\{ \frac{\delta \omega_j^{all}}{\sup_{k=1}^{n_{ip}} [\delta \omega_j(\mathbf{x}_k, t)]} \right\} \right) \tau_o$$

4. **while**  $ID_{tol} = \mathbf{false}$

5. Set  $\Delta t \leftarrow \Delta t / E_F$ :

$$({}_{t_{n+1}; \Delta t}) \mathfrak{M}(\phi)^* = {}_{t_n} \mathfrak{M}(\phi) + \Delta N \delta \tilde{\phi},$$

$$\Delta N = \frac{\Delta t}{\tau_o}, \quad \delta \tilde{\phi} = {}_{t_n} \tilde{\phi}(\mathbf{x}, \tau_o) - {}_{t_n} \tilde{\phi}(\mathbf{x}, 0)$$

6. Apply the macro-chronological external force increments and solve for  $({}_{t_{n+1}; \Delta t}) \mathfrak{M}(\phi)$ , using  $({}_{t_{n+1}; \Delta t}) \mathfrak{M}(\phi)^*$  as the initial values of a standard update procedure.

7. Solve micro-chronological IBVP for  $({}_{t_{n+1}; \Delta t}) \tilde{\phi}$  using  $({}_{t_{n+1}; \Delta t}) \mathfrak{M}(\phi)$

8. Set  $\Delta t \leftarrow \Delta t / 2$ , evaluate steps 5-7 in two increments to compute  $({}_{t_{n+1}; \Delta t / 2}) \mathfrak{M}(\phi)$  and  $({}_{t_{n+1}; \Delta t / 2}) \tilde{\phi}$

9. Compute  $({}_{t_{n+1}; \Delta t}) \boldsymbol{\omega}$  using  $({}_{t_{n+1}; \Delta t}) \mathfrak{M}(\phi)$  and  $({}_{t_{n+1}; \Delta t}) \tilde{\phi}$

10. Compute  $({}_{t_{n+1}; \Delta t / 2}) \boldsymbol{\omega}$  using  $({}_{t_{n+1}; \Delta t / 2}) \mathfrak{M}(\phi)$  and  $({}_{t_{n+1}; \Delta t / 2}) \tilde{\phi}$ .

11. Evaluate  $({}_{t_{n+1}; \Delta t}) \delta \boldsymbol{\omega}$  and  $({}_{t_{n+1}; \Delta t / 2}) \delta \boldsymbol{\omega}$  at each integration point.

- 12.

$$E_j^\omega = \sup_{k=1}^{n_{ip}} \left( \left\| ({}_{t_{n+1}; \Delta t}) \omega_j(\mathbf{x}_k, \tau) - ({}_{t_{n+1}; \Delta t / 2}) \omega_j(\mathbf{x}_k, \tau) \right\|_W \right); \quad \forall j \in 1, 2, \dots, n_{od}$$

$$\| \cdot \|_W = \int_0^{\tau_o} (\cdot)^W d\tau; \quad \text{if } 1 < W < \infty, \quad \| \cdot \|_W = \max(\cdot)(\mathbf{x}_k, \tau); \quad \text{if } W = \infty$$

13. **if**  $E_j^\omega \leq E_j^{tol}$ ;  $\forall j \in 1, 2, \dots, n_{od}$  **then**  $ID_{tol} \leftarrow \mathbf{true}$ ; **return**

14. **else**

$$E_F = \inf \left\{ \sup_{j=1}^{n_{od}} \frac{E_j^\omega}{E_j^{tol}}, E_L \right\}$$

**return**

15.  $t_{n+1} \leftarrow t_n + \Delta t$

(\*  $\boldsymbol{\omega}(\boldsymbol{\sigma}, \boldsymbol{\mu}, \mathbf{H})$  is the control variable vector for the adaptive time stepping algorithm. \*)

(\*  $n_{od}$  denotes the number of dimensions of the control variable vector. \*)

(\*  $\delta \boldsymbol{\omega}^{all}$  is the maximum allowable accumulation within a micro-chronological load cycle. \*)

(\*  $n_{ip}$  is the number of integration points. \*)

(\*  $\mathbf{E}^{tol}$  is the error tolerance vector for the control variables. \*)

(\*  $E_L$  defines the maximum allowable time step size reduction factor. \*)

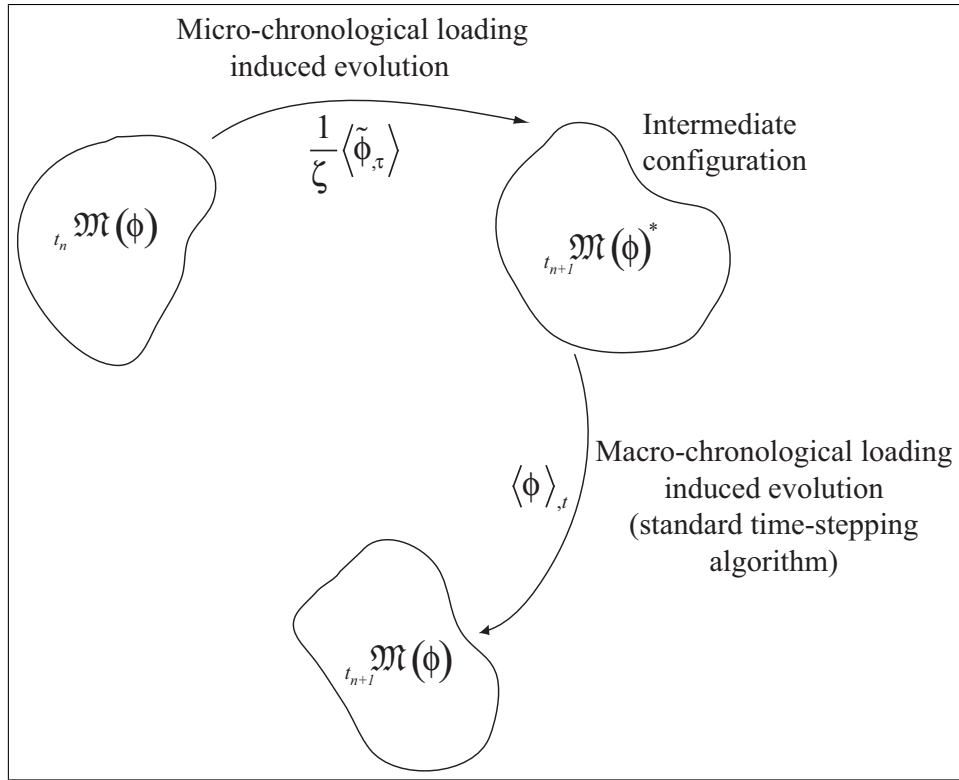


Figure 4: Schematic of the proposed two step update procedure.

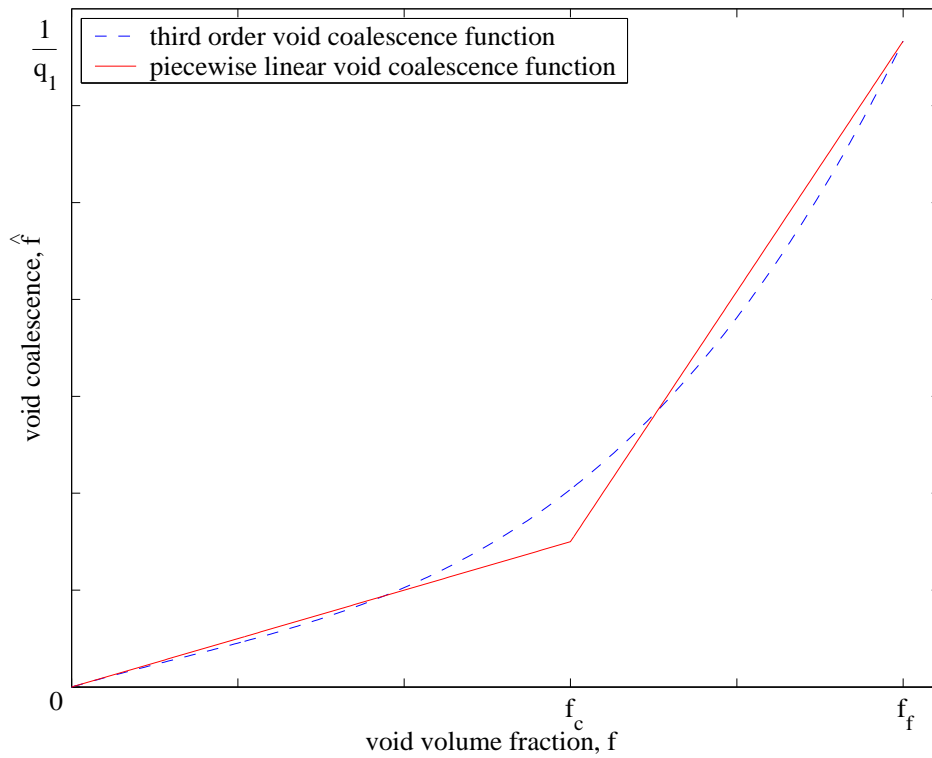


Figure 5: Comparison of the proposed third order and Tvergaard piecewise linear void coalescence functions.

Table 1: Material properties of the panel with a center crack.

Young's modulus, $E = 70 \text{ GPa}$	Poisson's ratio, $\nu = 0.3$	Initial yield stress $\sigma_Y = 231 \text{ MPa}$	Hardening parameter, $b = 0.0$
Tvergaard constants, $q_1 = 1.5$ $q_2 = 1.0$	Coalescence, $f_c = 0.15$ $f_f = 0.25$	Nucleation, $f_N = 0.04$ $s_N = 0.1$ $\epsilon_N = 0.3$	Hardening exponent, $n = 10$

## 6 Numerical Simulations

The performance of the proposed multiscale methodology is assessed by comparison to the direct cycle-by-cycle simulation. In the first example, a 20 cm-by-10 cm metal rectangular panel with a 10 mm long initial crack at its center is considered. The configuration of the panel with a center crack is presented in Fig. 6. The panel is subjected to the sinusoidal periodic loading in the vertical direction with constant amplitude of 0.0485 mm. The plane-strain geometry of the panel is discretized using 3-node triangular and 4-node quadrilateral elements as shown in Fig. 7. A quarter of the panel is considered due to symmetry.

The GTN model was employed to model the response of the material. The uniaxial stress-strain curve of the matrix material was modeled using a piecewise power law [28]:

$$\epsilon = \begin{cases} \frac{\sigma}{E} & \sigma \leq \sigma_Y \\ \frac{\sigma_Y}{E} \left( \frac{\sigma}{\sigma_Y} \right)^n & \sigma > \sigma_Y \end{cases} \quad (62)$$

where, the material parameter,  $n$ , is the strain hardening exponent. Table 1 summarizes the material properties used. The material is assumed to have a small initial void volume fraction,  $f_0 = 0.00531$ .

Figure 8 depicts the crack growth curves in the panel as computed by the proposed multiscale method and the reference cycle-by-cycle approach. The multiscale simulations were performed with algorithm parameters,  $E_L = 4$ ,  $\delta\omega^{all} = \{0.02, 0.02\}$ , and with error tolerances,  $\mathbf{E}^{tol} = \{0.001, 0.0015\}$  (simulation ms1) and  $\mathbf{E}^{tol} = \{0.0025, 0.003\}$  (simulation ms2). The reference solution is obtained by simulating each cycle of the loading history. Figure 8 shows the convergence of the multiscale solution to the reference (cycle-by-cycle simulation) solution when the error tolerance is reduced. The computational cost is evaluated based on the number of resolved load cycles. In the cycle-by-cycle approach we simulated 720 load cycles, whereas multiscale simulations ms1 and ms2 required 179 and 165 cycles, respectively. Figure 9 shows the evolution of the void volume fraction, and vertical components of the stress and plastic strain tensors within the element at the crack tip for the first 200 cycles (after which the element vanished). A reasonable agreement was observed between the response fields computed using the reference solution and the proposed multiscale method (simulation ms1).

Next, the fatigue response of the rubber-modified epoxy (RME) adhesives was investigated. Figure 10 illustrates the fracture behavior of a scarf joint made of an epoxy adhesive subjected to the uniaxial monotonic tensile loading [50]. Inclusion of rubber particles in epoxy resins is used to increase the ductility of the adhesive [51]. The Gurson type model is reasonably well suited to idealize the response characteristics of the RME adhesives as proposed by a number of recent publications (e.g., [51, 52, 53]).

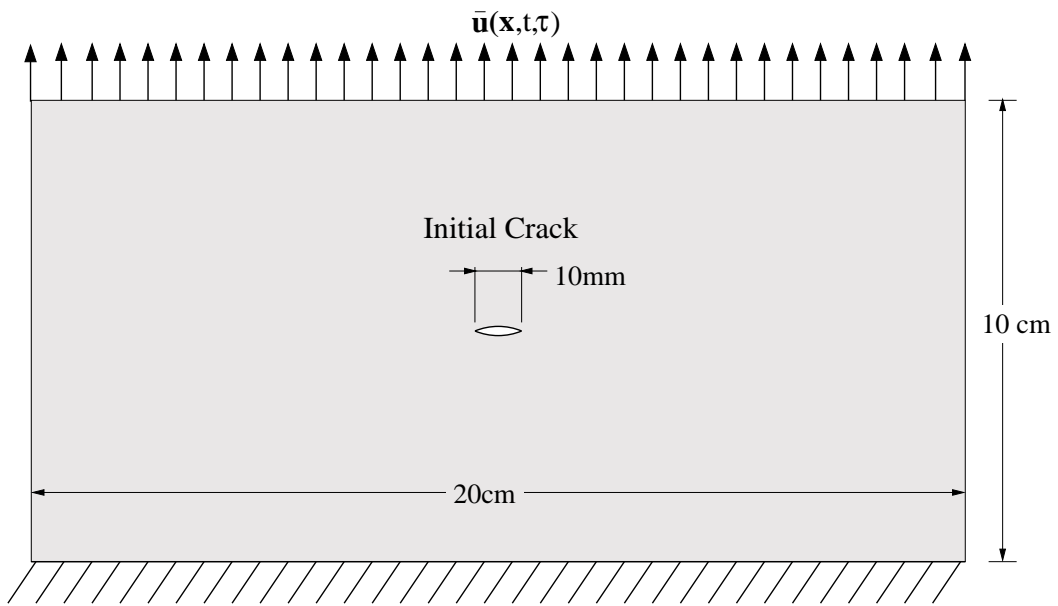


Figure 6: Configuration of the panel with a center crack.

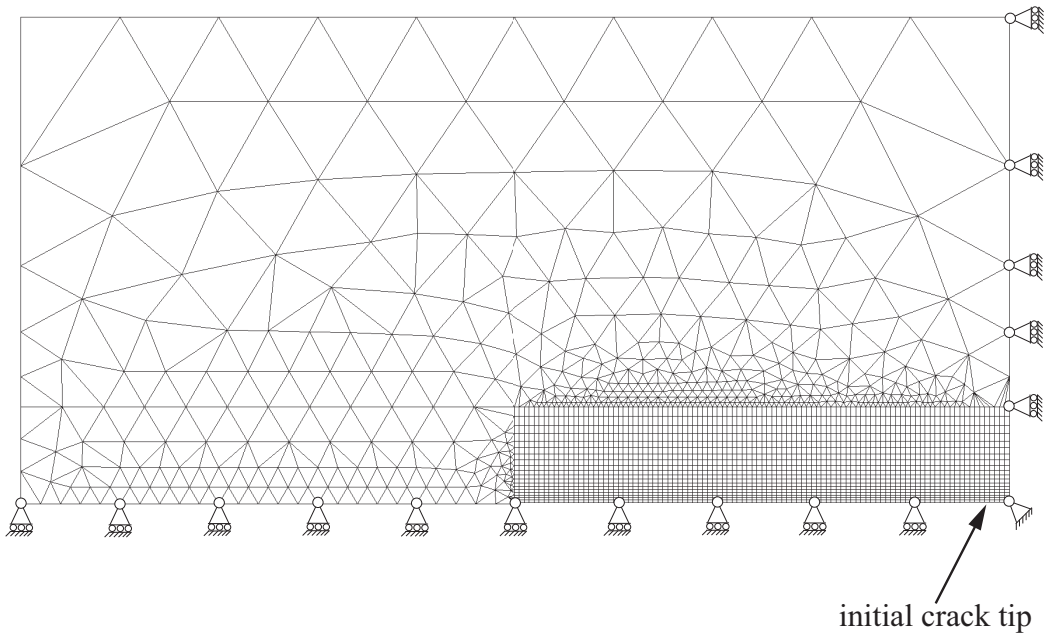


Figure 7: Finite element mesh of the panel with a center crack.

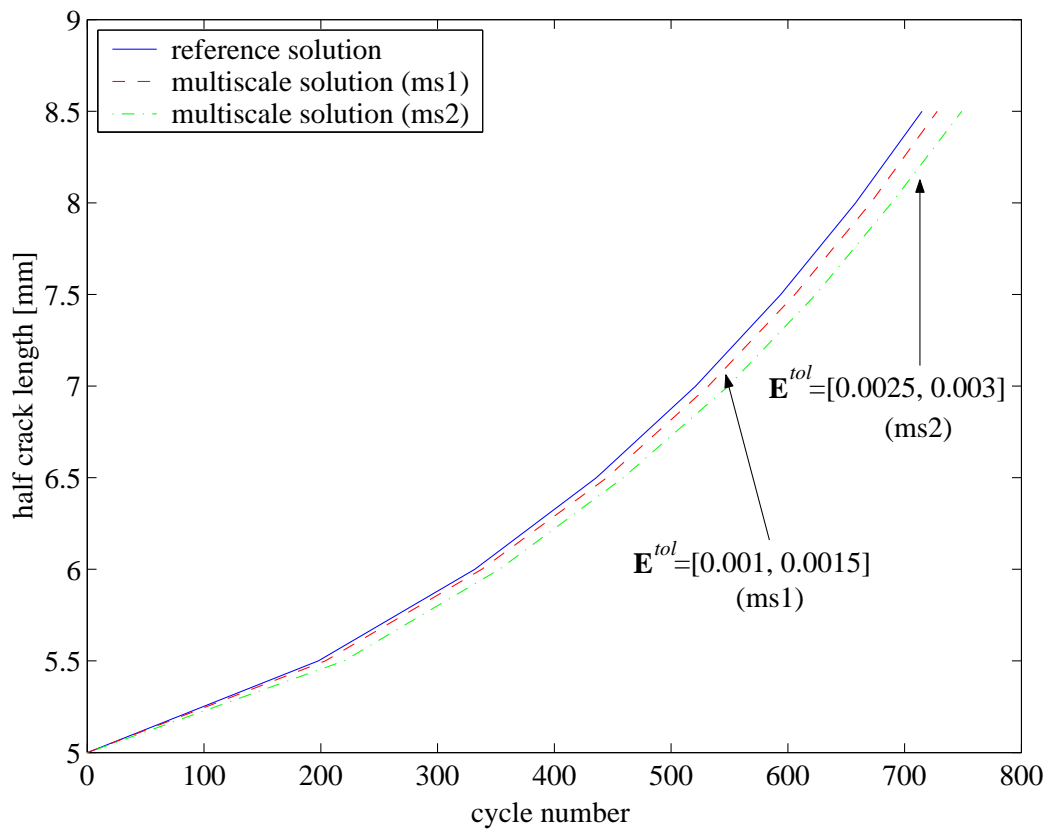


Figure 8: Crack growth curve of the panel with a center crack.

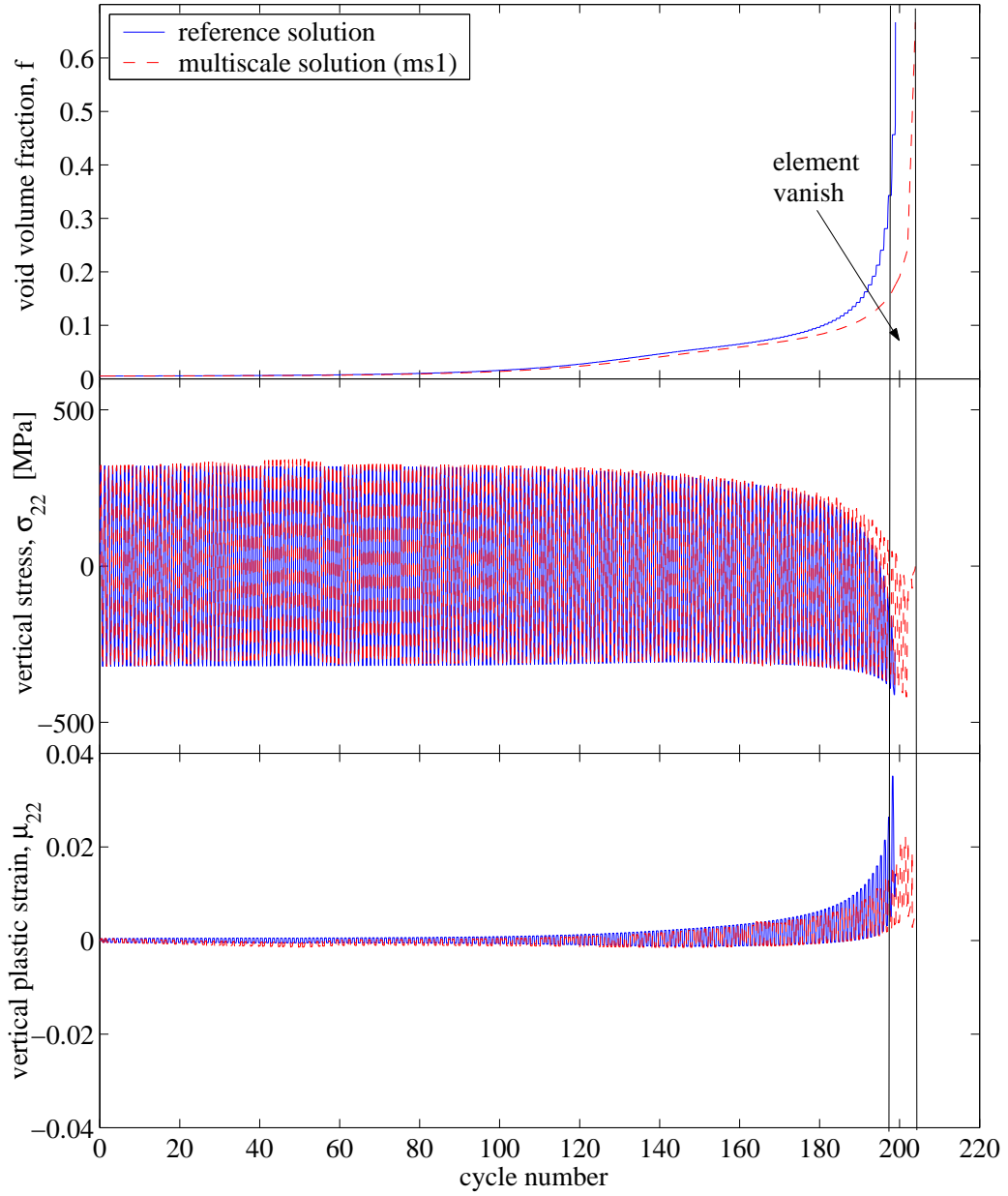


Figure 9: Evolution of void volume fraction, vertical stress and plastic strain at the tip of the crack (crack length: 5 cm) for the panel with a center crack.

Table 2: Material properties of the adherent and adhesive in the plate with a scarf joint.

	Young's modulus, $E$ [GPa]	Poisson's ratio, $\nu$	Initial yield stress, $\sigma_Y$ [MPa]	Hardening $b = 0.0$ $n = 10.0$	Tvergaard constants $q_1 = 1.9$ $q_2 = 1.0$
Epoxy resin	3	0.33	40		
Adherent	200	0.3			

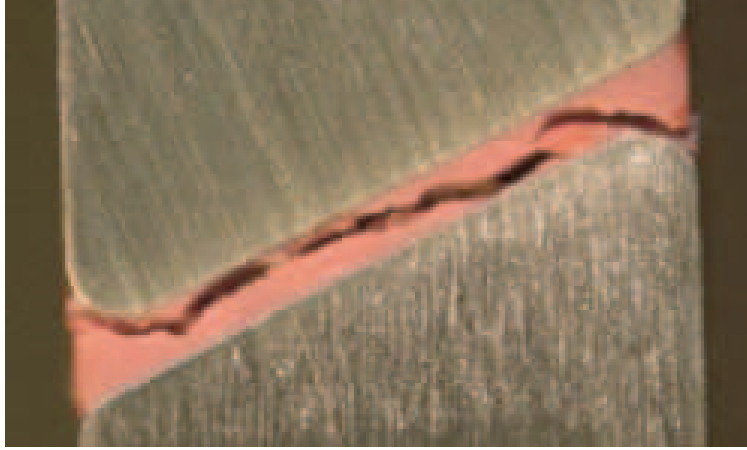


Figure 10: Crack path of the RME adhesive layer after a monotonic uniaxial tensile test. Courtesy of the National Physical Laboratory, UK.

A plane-strain material model for the rectangular plate (1-by-2 horizontal to vertical ratio) with a  $28^\circ$  angle (to the horizontal) scarf joint is considered (Fig. 11). The thickness of the joint is 5% of the length of the plate. The adherent is assumed to behave elastically under the applied loading and the GTN model is chosen to model the adhesive layer. The material properties of the RME adhesive and adherent are provided in Table 2. The uniaxial stress-strain curve of the matrix material is modeled by (62). The initial volume fraction of the rubber inclusions (i.e.,  $f_0$ ) is taken to be 17%. Void nucleation and coalescence effects were ignored. A small initial flaw was introduced at the two ends of the joint.

Figure 12 illustrates the evolution of void volume fraction within a number of selected elements in front of the crack tip. The multiscale simulation was conducted using the algorithm parameters,  $E_L = 4$ ,  $\delta\omega^{all} = \{0.02, 0.02\}$ , and with error tolerance,  $\mathbf{E}^{tol} = \{0.0004, 0.0005\}$ . Snapshots of the crack growth history for the cycle-by-cycle and multiscale techniques are compared in Fig. 13. A good agreement in the overall crack growth was observed between the reference and the multi-scale approach, despite some discrepancies in the void volume fraction growth in the individual elements. The simulated crack path under cyclic loading conditions was found to be somewhat smoother compared to the test data under monotonic loading (Fig. 10). This trend is consistent with experimental observations [54].

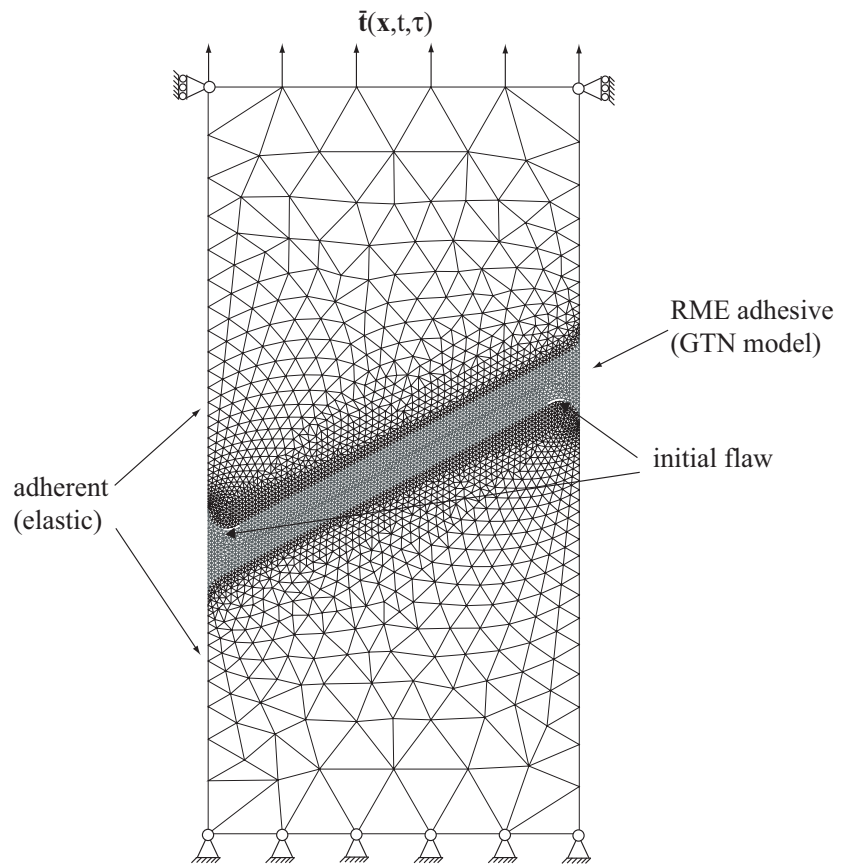


Figure 11: Finite element mesh of the plate with a scarf joint.

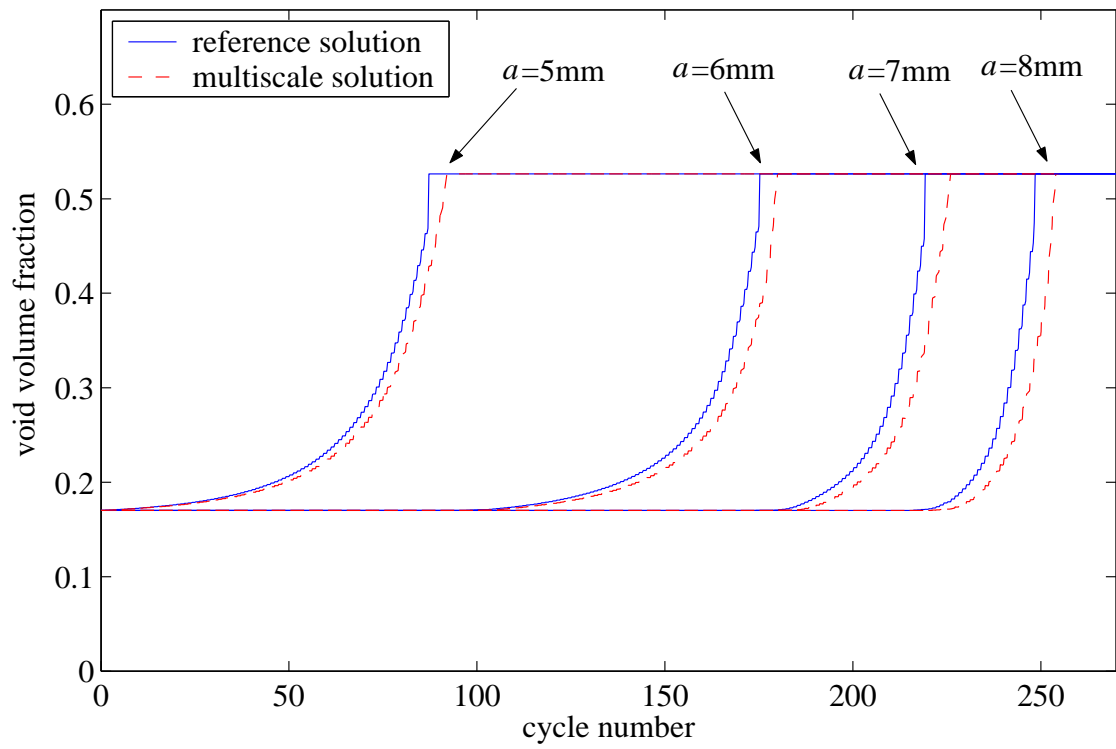


Figure 12: Evolution of the void volume fraction within selected elements during the first 260 cycles computed by reference and multiscale techniques for the plate with a scarf joint.

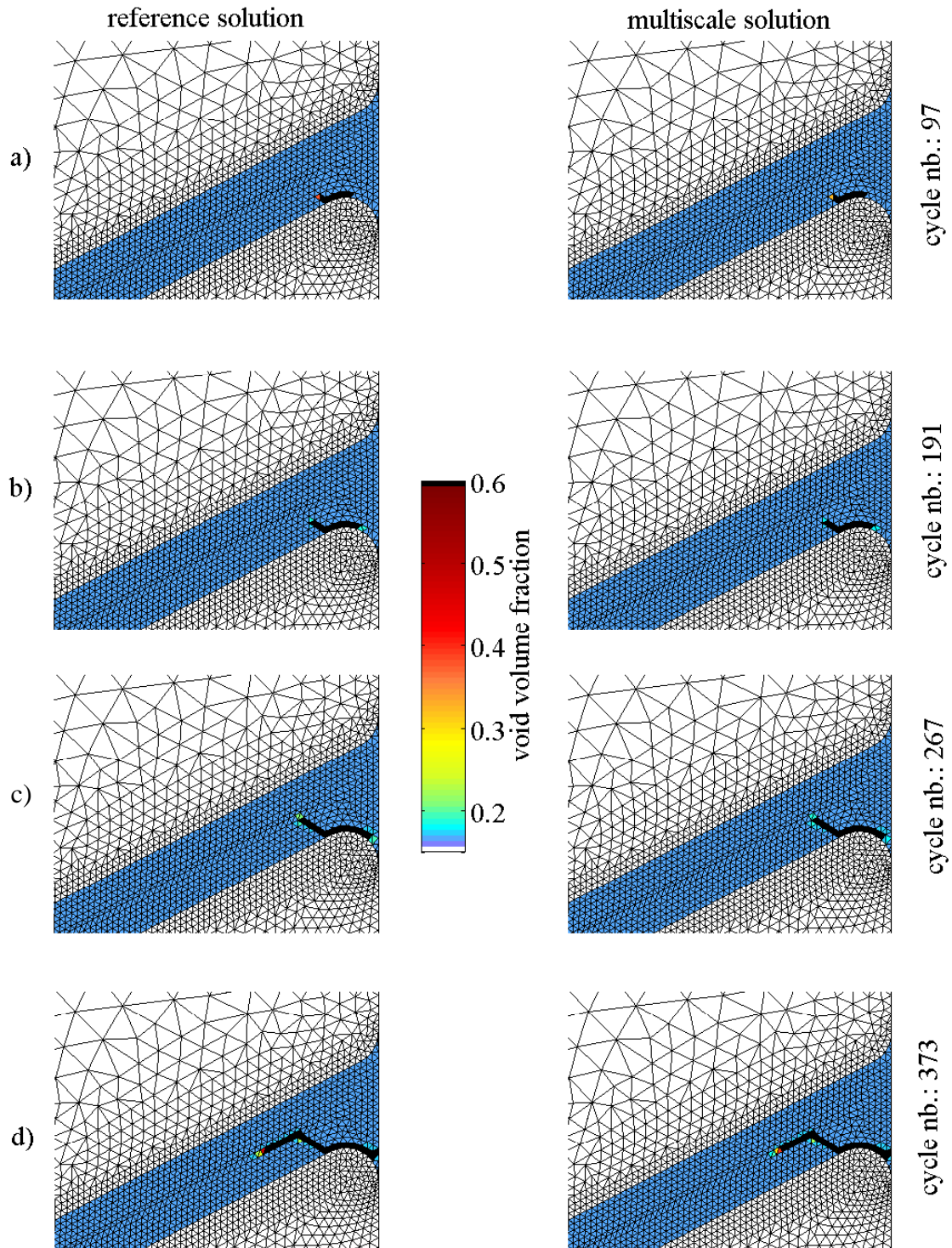


Figure 13: Crack propagation patterns of the plate with a scarf joint after (a) 97, (b) 161, (c) 267, and (d) 373 load cycles, as computed by the reference and multiscale techniques.

## 7 Conclusion

A multiscale fatigue model was developed within the new framework of the mathematical homogenization theory for almost periodic fields. The almost-periodic operators have been introduced to capture the long time response of inelastic solids subjected to short duration oscillatory loading. The proposed life prediction methodology was implemented in ABAQUS and has been found to be in good agreement with the direct cycle-by-cycle simulations.

This work represents the first attempt in developing a simulation-based approach in the field where the design is dominated by experiments. Several theoretical issues, such as mesh sensitivity, as well as the critical issue of validation (against the experimental data) have not been addressed so far. These issues remain the focus of our future studies.

## 8 Acknowledgement

This work was supported by the Office of Naval Research through grant number N00014-97-1-0687. This support is gratefully acknowledged. Figure 10: © Crown copyright 2004. Reproduced by permission of the Controller of HMSO.

## References

- [1] P. C. Paris and F. Erdogan. A critical analysis of crack propagation laws. *J. Basic Engng.*, 85:528–534, 1963.
- [2] M. H. El Haddad, T. H. Topper, and K. N. Smith. Prediction of non-propagating cracks. *Engng. Fracture Mech.*, 11:573–584, 1979.
- [3] W. Elber. Fatigue crack closure under cyclic tension. *Engng. Fracture Mech.*, 2:37–45, 1970.
- [4] R. G. Foreman, V. E. Keary, and R. M. Engle. Numerical analysis of crack propagation in cyclic-loaded structures. *J. Basic Engng.*, 89:459–464, 1967.
- [5] M. Klesnil and P. Lukas. Influence of strength and stress history on growth and stabilisation of fatigue cracks. *Engng. Fracture Mech.*, 4:77–92, 1972.
- [6] O. E. Wheeler. Spectrum loading and crack growth. *J. Basic Engng.*, 94:181–186, 1972.
- [7] O. Nguyen, E. A. Repetto, M. Ortiz, and R. A. Radovitzky. A cohesive model of fatigue crack growth. *Int. J. Fracture*, 110(4):351–369, 2001.
- [8] K. L. Roe and T. Siegmund. An irreversible cohesive zone model for interface fatigue crack growth simulation. *Engng. Fracture Mech.*, 70:209–232, 2003.
- [9] J. L. Chaboche. Continuum damage mechanics I: General concepts & II: Damage growth, crack initiation and crack growth. *J. Appl. Mech.*, 55:59–72, 1988.
- [10] C. L. Chow and Y. Wei. A model of continuum damage mechanics for fatigue failure. *Int. J. Fatigue*, 50:301–306, 1991.

- [11] J. Fish and Q. Yu. Computational mechanics of fatigue and life predictions for composite materials and structures. *Comp. Meth. Appl. Mech. Engng.*, 191:4827–4849, 2002.
- [12] C. Oskay and J. Fish. Fatigue life prediction using 2-scale temporal asymptotic homogenization. *Int. J. Numer. Meth. Engng.*, 2003. in print.
- [13] M. Kaminski and M. Kleiber. Numerical homogenization of N-component composites including stochastic interface defects. *Int. J. Numer. Meth. Engng.*, 47:1001–1027, 2000.
- [14] G. W. Milton. *The Theory of Composites*. Cambridge Univ. Press, Cambridge, UK, 2002.
- [15] S. Torquato. *Random Heterogeneous Materials: Microstructure and Macroscopic Properties*. Springer-Verlag, New York, 2002.
- [16] K. Sab. On the homogenization and the simulation of random materials. *Eur. J. Mech., A/Solids*, 11:585–607, 1992.
- [17] J. Fish and A. Wagiman. Multiscale finite element method for a locally nonperiodic heterogeneous medium. *Comp. Mech.*, 12:164–180, 1993.
- [18] S. Ghosh, K. Lee, and S. Moorthy. Multiple scale analysis of heterogeneous elastic structures using homogenization theory and Voronoi cell finite element method. *Int. J. Solids Structures*, 32:27–62, 1995.
- [19] S. Ghosh, K. Lee, and S. Moorthy. Two scale analysis of heterogeneous elastic-plastic materials with asymptotic homogenization and Voronoi cell finite element method. *Comput. Methods Appl. Mech. Engng.*, 132:63–116, 1996.
- [20] J. T. Oden and T. I. Zohdi. Analysis and adaptive modeling of highly heterogeneous elastic structures. *Comput. Methods. Appl. Mech. Engng.*, 148:367–391, 1997.
- [21] T. I. Zohdi, J. T. Oden, and G. J. Rodin. Hierarchical modeling of heterogeneous bodies. *Comput. Meth. Appl. Mech. Engng.*, 138:273–298, 1996.
- [22] M.-J. Pindera, J. Aboudi, and S. M. Arnold. Limitations of the uncoupled, RVE-based micromechanical approach in the analysis of functionally graded composites. *Mechanics of Materials*, 20:77–94, 1995.
- [23] N. Ansini and A. Braides. Separation of scales and almost-periodic effects in the asymptotic behavior of perforated media. *Acta Applicandae Math.*, 65:59–81, 2001.
- [24] A. Braides and A. Defranceschi. *Homogenization of Multiple Integrals*. Oxford Univ. Press, Oxford, 1998.
- [25] G. Nguetseng and H. Nnang. Homogenization of nonlinear monotone operators beyond the periodic setting. *Electronic J. Diff. Eqn.*, 36:1–24, 2003.
- [26] O. A. Oleinik, A. S. Shamaev, and G. A. Yosifian. *Mathematical Problems in Elasticity and Homogenization*. North-Holland Press, Amsterdam, 1992.

- [27] V. V. Zhikov, S. M. Kozlov, and O. A. Oleinik. *Homogenization of Differential Operators and Integral Functionals*. Springer-Verlag, New York, 1994.
- [28] V. Tvergaard. Material failure by void growth to coalescence. *Adv. Appl. Mech.*, 27:83–151, 1990.
- [29] Z. P. Bazant, T. B. Belytschko, and T. P. Chang. Continuum theory for strain softening. *J. Engng. Mech.*, 110:1666–1691, 1984.
- [30] R. de Borst and L. J. Sluys. Localization in Cosserat continuum under static and dynamic loading conditions. *Comput. Methods Appl. Mech. Engng.*, 90:805–827, 1991.
- [31] R. de Borst and H. B. Muhlhaus. Gradient dependent plasticity: Formulation and algorithmic aspects. *Int. J. Numer. Meth. Engng.*, 35:521–539, 1992.
- [32] K. Garikipati and T. J. R. Hughes. A variational multiscale approach to strain localization formulation for multidimensional problems. *Comput. Methods Appl. Mech. Engng.*, 188:39–60, 2000.
- [33] J. C. Simo and J. Oliver. A new approach to the analysis and simulation of strain softening in solids. In Z. P. Bazant, Z. Bittnar, M. Jirasek, and J. Mazars, editors, *Fracture and Damage in Quasibrittle Structures*. 1994.
- [34] A. Benssousan, J. L. Lions, and G. Papanicolaou. *Asymptotic Analysis for Periodic Structures*. North-Holland, Amsterdam, 1978.
- [35] D. Cioranescu and P. Donato. *An Introduction to Homogenization*. Oxford Univ. Press, Oxford, UK, 1999.
- [36] A. L. Gurson. Continuum theory of ductile rapture by void nucleation and growth: Part I—yield criteria and flow rules for porous ductile media. *J. Engng. Mater. and Technol.*, 99:2–15, 1977.
- [37] V. Tvergaard. Influence of voids on shear band instabilities under plane strain conditions. *Int. J. Fracture*, 17:389–407, 1981.
- [38] V. Tvergaard. On localization in ductile materials containing spherical voids. *Int. J. Fracture*, 18:237–252, 1982.
- [39] C. C. Chu and A. Needleman. Void nucleation effects in biaxially stretched sheets. *J. Engng. Mater. and Technol.*, 102:249–256, 1980.
- [40] V. Tvergaard. Material failure by void coalescence in localized shear bands. *Int. J. Solids Structures*, 18:659–672, 1982.
- [41] M. E. Mear and J. W. Hutchinson. Influence of yield surface curvature on flow localization in dilatant plasticity. *Mech. Mater.*, 4:395–407, 1985.
- [42] V. Tvergaard. Effect of yield surface curvature and void nucleation on plastic flow localization. *J. Mech. Phys. Solids*, 35(1):43–60, 1987.

- [43] M. Gologanu, J.-B. Leblond, G. Perrin, and J. Devaux. *Recent Extensions of Gurson's Model for Porous Ductile Metals*, chapter 2, pages 61–130. Springer-Verlag, 1997.
- [44] V. Tvergaard and A. Needleman. Analysis of the cup-cone fracture in a round tensile bar. *Acta Metall.*, 32(1):157–169, 1984.
- [45] J. Llorca, S. Suresh, and A. Needleman. An experimental and numerical study of cyclic deformation in metal-matrix composites. *Metall. Trans. A*, 23A:919–934, 1992.
- [46] M. Ristinmaa. Void growth in cyclic loaded porous plastic solid. *Mech. of Mater.*, 26:227–245, 1997.
- [47] N. Aravas. On the numerical integration of a class of pressure-dependent plasticity models. *Int. J. Numer. Meth. Engng.*, 24:1395–1416, 1987.
- [48] J. H. Lee and Y. Zhang. On the numerical integration of a class of pressure-dependent plasticity models with mixed hardening. *Int. J. Numer. Meth. Engng.*, 32:419–438, 1991.
- [49] J. C. Simo and T. J. R. Hughes. *Computational Inelasticity*. Springer, New York, 1998.
- [50] G. Dean, L. Crocker, B. Read, and L. Wright. Prediction of deformation and failure of rubber-toughened adhesive joints. *Int. J. Adhes. Adhes.*, 24:295–306, 2004.
- [51] M. Imanaka and Y. Suzuki. Yield behavior of rubber-modified epoxy adhesives under multi-axial stress conditions. *J. Adhesion Sci. Technol.*, 16(12):1687–1700, 2002.
- [52] R. S. Kody and A. J. Lesser. Yield behavior and energy absorbing characteristics of rubber-modified epoxies subjected to biaxial stress states. *Polym. Comp.*, 20:250–259, 1999.
- [53] A. Lazzeri and C. B. Bucknall. Dilatation bands in rubber toughened plastics. *J. Mater. Sci.*, 28:6799–6808, 1993.
- [54] N. E. Frost, K. J. Marsh, and L. P. Pook. *Metal Fatigue*. Clarendon Press, Oxford, 1974.

## A Micro- and macro-chronological evolution equations for the GTN model

The plastic loading parameter,  $H$ , is computed by considering a fictitious yield surface,  $\Phi^G$  [41, 42]:

$$\Phi^G = \Phi^G(\boldsymbol{\sigma}^G, f, \sigma_M) = \frac{(q^G)^2}{\sigma_M^2} + 2q_1 \hat{f} \cosh\left(-\frac{3}{2}q_2 \frac{p^G}{\sigma_M}\right) - 1 - (q_1 \hat{f})^2 \quad (63)$$

and, choosing the fictitious stress components,  $\boldsymbol{\sigma}^G$ , such that:

$$\frac{\boldsymbol{\sigma}^G}{\sigma_M} = \frac{\boldsymbol{\Theta}}{\sigma_F} \quad (64)$$

The above equation ensures that  $\Phi = 0$  implies  $\Phi^G = 0$ . The micro-chronological plastic strain rate tensor,  $\boldsymbol{\mu}_{,\tau}$ , is chosen to be equivalent to the associated fictitious plastic strain rate tensor,  $\boldsymbol{\mu}_{,\tau}^G$ . Using (43), (45) and (64),  $H$  can be determined as:

$$H = -\frac{\sigma_M}{\sigma_F} \left\{ \frac{\partial \Phi}{\partial f} (1-f) \left( \boldsymbol{\delta} : \frac{\partial \Phi}{\partial \boldsymbol{\sigma}} \right) + \left[ \frac{\sigma_M}{\sigma_F} \mathcal{A} \frac{\partial \Phi}{\partial f} + \frac{\partial \Phi}{\partial \sigma_F} \right] \frac{E^t}{1-f} \frac{1}{\sigma_M} \left( \boldsymbol{\Theta} : \frac{\partial \Phi}{\partial \boldsymbol{\sigma}} \right) \right\} \quad (65)$$

The macro-chronological consistency parameter,  $\lambda^o$ , is evaluated by setting the macro-chronological plastic strain rate tensor,  $\boldsymbol{\mu}_{,t}$  to be equivalent to the associated fictitious plastic strain rate tensor,  $\boldsymbol{\mu}_{,t}^G$ .

The micro- and macro-chronological evolution equations of void volume fraction, equivalent plastic strain, matrix flow strength, and yield surface radius are obtained by substituting the state variable and stress decompositions into (25), (26), (28), (29), and (22), matching the terms with respect to their orders, and applying the PTH operator to the higher order equations. The original evolution equation of the void volume fraction yields (for tensile loading):

$$O(\zeta^{-1}) : \quad \tilde{f}_{,\tau} = (1 - \mathfrak{M}(f) - \tilde{f}) \boldsymbol{\delta} : \tilde{\boldsymbol{\mu}}_{,\tau} + \mathcal{A} \tilde{\rho}_{,\tau} \quad (66)$$

$$O(1) : \quad f_{,t}^o = (1 - f^o) \boldsymbol{\delta} : \boldsymbol{\mu}_{,t}^o - \langle \tilde{f} \boldsymbol{\delta} : \boldsymbol{\mu}_{,t}^1 \rangle + \langle \mathcal{A} \rangle \rho_{,t}^o + \langle \mathcal{A} \rho_{,t}^1 \rangle \quad (67)$$

The micro-chronological evolution equation for the void volume fraction is given by (66). Exploiting the dual decomposition relations, the evolution equation of void volume fraction for the macro-chronological problem yields:

$$\begin{aligned} \mathfrak{M}(f)_{,t} = \frac{1}{\zeta} \langle \tilde{f}_{,\tau} \rangle + f_{,t}^o = (1 - \mathfrak{M}(f) - \langle \tilde{f} \rangle) \boldsymbol{\delta} : \mathfrak{M}(\boldsymbol{\mu})_{,t} - \left\langle \tilde{f} \boldsymbol{\delta} : \left( \frac{1}{\zeta} \tilde{\boldsymbol{\mu}}_{,\tau} + \tilde{\boldsymbol{\mu}}_{,t} \right) \right\rangle \\ + \langle \mathcal{A} \rangle \mathfrak{M}(\rho)_{,t} - \left\langle \mathcal{A} \left( \frac{1}{\zeta} \tilde{\rho}_{,\tau} + \tilde{\rho}_{,t} \right) \right\rangle \end{aligned} \quad (68)$$

Similarly, the original evolution equation for the equivalent plastic strain may be expressed in terms of the decompositions given in (32):

$$O(\zeta^{-1}) : \quad \tilde{\rho}_{,\tau} = \frac{(\mathfrak{M}(\boldsymbol{\Theta}) + \tilde{\boldsymbol{\Theta}}) : \tilde{\boldsymbol{\mu}}_{,\tau}}{[1 - \mathfrak{M}(f) - \tilde{f}] [\mathfrak{M}(\sigma_F) + \tilde{\sigma}_F]} \quad (69)$$

$$\begin{aligned} O(1) : \quad \rho_{,t}^o = \left\langle \frac{(\mathfrak{M}(\boldsymbol{\Theta}) + \tilde{\boldsymbol{\Theta}})}{[1 - \mathfrak{M}(f) - \tilde{f}] [\mathfrak{M}(\sigma_F) + \tilde{\sigma}_F]} \right\rangle : \boldsymbol{\mu}_{,t}^o \\ + \left\langle \frac{(\mathfrak{M}(\boldsymbol{\Theta}) + \tilde{\boldsymbol{\Theta}}) : \boldsymbol{\mu}_{,t}^1}{[1 - \mathfrak{M}(f) - \tilde{f}] [\mathfrak{M}(\sigma_F) + \tilde{\sigma}_F]} \right\rangle \end{aligned} \quad (70)$$

The micro-chronological evolution equation for the equivalent plastic strain is given by (69). The macro-chronological equation takes the form:

$$\begin{aligned} \mathfrak{M}(\rho)_{,t} = \frac{1}{\zeta} \langle \tilde{\rho}_{,\tau} \rangle + \rho_{,t}^o = & \left\langle \frac{(\mathfrak{M}(\Theta) + \tilde{\Theta})}{[1 - \mathfrak{M}(f) - \tilde{f}] [\mathfrak{M}(\sigma_F) + \tilde{\sigma}_F]} \right\rangle : \mathfrak{M}(\mu)_{,t} \\ & + \left\langle \frac{(\mathfrak{M}(\Theta) + \tilde{\Theta})}{[1 - \mathfrak{M}(f) - \tilde{f}] [\mathfrak{M}(\sigma_F) + \tilde{\sigma}_F]} : \left( \frac{1}{\zeta} \tilde{\mu}_{,\tau} + \tilde{\mu}_{,t} \right) \right\rangle \end{aligned} \quad (71)$$

The evolution equations of the matrix flow strength and the yield surface radius may be expressed as:

$$O(\zeta^{-1}) : \quad \tilde{\sigma}_{M,\tau} = E^t \tilde{\rho}_{,\tau}; \quad \tilde{\sigma}_{F,\tau} = b \tilde{\sigma}_{M,\tau} \quad (72)$$

$$O(1) : \quad \sigma_{M,t}^o = \langle E^t \rangle \rho_{,t}^o + \langle E^t \rho_{,t}^1 \rangle; \quad \sigma_{F,t}^o = b \sigma_{M,t}^o \quad (73)$$

and,

$$\mathfrak{M}(\sigma_M)_{,t} = \frac{1}{\zeta} \langle \tilde{\sigma}_{M,\tau} \rangle + \sigma_{M,t}^o = \langle E^t \rangle \mathfrak{M}(\rho)_{,t} + \left\langle E^t \left( \frac{1}{\zeta} \tilde{\rho}_{,\tau} + \tilde{\rho}_{,t} \right) \right\rangle \quad (74)$$

$$\mathfrak{M}(\sigma_F)_{,t} = \frac{1}{\zeta} \langle \tilde{\sigma}_{F,\tau} \rangle + \sigma_{F,t}^o = b \mathfrak{M}(\sigma_M)_{,t} \quad (75)$$

in which, (72a) and (74) are the micro- and macro-chronological evolution equations of the matrix flow strength, respectively. (72b) and (75) correspond to the evolution equations of the yield surface radius for the micro- and macro-chronological problems, respectively.

The consistency parameter for the kinematic hardening rule,  $\vartheta$ , is decomposed using an expansion similar to the expansion of  $\lambda$ :

$$\vartheta(t, \tau) = \frac{1}{\zeta} \vartheta^1(t, \tau) + \vartheta^o(t) \quad (76)$$

where,  $\vartheta^1$ , and  $\vartheta^o$  may be interpreted as the consistency parameters of the hardening rule induced by the micro- and macro-chronological loadings, respectively. Applying (32) to the yield surface radius, inserting the resulting equation and (76) into (31), separating the terms with respect to their orders, and applying (8) to the resulting  $O(1)$  equation, we obtain:

$$O(\zeta^{-1}) : \quad \tilde{\alpha}_{,\tau} = \vartheta^1 (\mathfrak{M}(\Theta) + \tilde{\Theta}) \quad (77)$$

$$O(1) : \quad \alpha_{,t}^o = \vartheta^o \Theta^o \quad (78)$$

The micro-chronological evolution equation for the center of the yield surface,  $\alpha^1$ , is given by (77). The micro-chronological consistency parameter,  $\vartheta^1$ , is evaluated using the consistency condition (43):

$$\vartheta^1 = Q \frac{\partial \Phi}{\partial \sigma} : \tilde{\sigma}_{,\tau} \quad (79)$$

where  $Q$  is expressed as:

$$Q = (1 - b) \left( \Theta : \frac{\partial \Phi}{\partial \sigma} \right)^{-1} \left[ 1 + \frac{\sigma_y}{\sigma_F} \frac{1}{H} \frac{\partial \Phi}{\partial f} \left\{ (1 - f) \left( \delta : \frac{\partial \Phi}{\partial \sigma} \right) + \frac{E^t}{1 - f} \frac{1}{\sigma_F} \left( \Theta : \frac{\partial \Phi}{\partial \sigma} \right) \right\} \right] \quad (80)$$

The evolution equation for the macro-chronological yield surface center is evaluated using the definition of the APTH operator:

$$\mathfrak{M}(\boldsymbol{\alpha})_{,t} = \frac{1}{\zeta} \langle \vartheta^1 (\mathfrak{M}(\boldsymbol{\Theta}) + \tilde{\boldsymbol{\Theta}}) \rangle + \vartheta^0 (\mathfrak{M}(\boldsymbol{\Theta}) + \langle \tilde{\boldsymbol{\Theta}} \rangle) \quad (81)$$

The macro-chronological consistency parameter for the hardening rule,  $\vartheta^0$ , is evaluated by applying the PTH operator to (44):

$$\vartheta^0 = \left\langle \mathcal{Q} \frac{\partial \Phi}{\partial \boldsymbol{\sigma}} \right\rangle : \mathfrak{M}(\boldsymbol{\sigma})_{,t} + \left\langle \mathcal{Q} \frac{\partial \Phi}{\partial \boldsymbol{\sigma}} : \tilde{\boldsymbol{\sigma}}_{,t} \right\rangle \quad (82)$$